



# Recent Progress Toward Imaging Application of Multifunction Sonosensitizers in Sonodynamic Therapy

Chunyu Wang , Yuhang Tian, Bolin Wu, Wen Cheng 

Department of Ultrasound, Harbin Medical University Cancer Hospital, Harbin, People's Republic of China

Correspondence: Wen Cheng; Bolin Wu, Department of Ultrasound, Harbin Medical University Cancer Hospital, No. 150, Haping Road, Nangang District, Harbin, 150081, People's Republic of China, Tel +86 13313677182; +86 15663615088, Fax +86 451 85718392; +86 451 86298651, Email [chengwen@hrbmu.edu.cn](mailto:chengwen@hrbmu.edu.cn); [wubolin@hrbmu.edu.cn](mailto:wubolin@hrbmu.edu.cn)

**Abstract:** Sonodynamic therapy (SDT) is a rapidly developing non-surgical therapy that initiates sensitizers' catalytic reaction using ultrasound, showing great potential for cancer treatment due to its high safety and non-invasive nature. In addition, recent research has found that using different diagnostic and therapeutic methods in tandem can lead to better anticancer outcomes. Therefore, as essential components of SDT, sonosensitizers have been extensively explored to optimize their functions and integrate multiple medical fields. The review is based on five years of articles evaluating the combined use of SDT and imaging in treating cancer. By developing multifunctional sonosensitive particles that combine imaging and sonodynamic therapy, we have integrated diagnosis into the treatment of precision medicine applications, improving SDT cell uptake and antitumor efficacy utilizing different tumour models. This paper describes the imaging principle and the results of cellular and animal imaging of the multifunctional sonosensitizers. Efforts are made in this paper to provide data and design references for future SDT combined imaging research and clinical application development and to provide offer suggestions.

**Keywords:** sonodynamic therapy, multifunctional sonosensitizers, imaging, ultrasound

## Introduction

Worldwide, cancer leads the list of causes of death, and the mortality and morbidity associated with cancer are on the rise.<sup>1</sup> Although cancer research is expensive, cancer's variety, heterogeneity and complexity limit therapeutic choices.<sup>2</sup> Surgery, radiation and chemotherapy have systemic toxicity, selectivity, pharmacoresistance and possible long-term effects. Various remedies have been explored to compensate for these shortcomings.<sup>3</sup> SDT is a rapidly evolving, updated therapy with excellent development potential.

SDT employs low-frequency ultrasound to irradiate sonosensitive substances concentrated in the treatment region to achieve the therapeutic goal of destroying aberrant cells via the toxic and physical effects.<sup>4</sup> Ultrasound (US) has a high tissue penetration rate and can operate on tumor cells deep into biological tissues. The therapeutic impact can be improved by using concentrated ultrasonic energy and a dynamic effect.<sup>3</sup> Ultrasonic waves can cause the formation of bubbles in the liquid. The bubbles then sharply shrink and break to produce mechanical damage, local high temperature and sonoluminescence, which is called inertial cavitation.<sup>5,6</sup> Inertial cavitation can produce reactive oxygen species (ROS) by directly decomposing the sonosensitizers or through pyrolysis with water.<sup>7</sup> The resulting ROS will further react with other endogenous substrates to form alkoxy and peroxy radicals.<sup>8</sup> All of these adverse factors can lead to cell death, including autophagy, apoptosis, necroptosis, and pyroptosis, and limit tumor spread in sonodynamic treatment for various malignancies (Figure 1).<sup>9–15</sup> This method, in particular, allows for precision tumor targeting while causing minimal harm to the surrounding normal tissue.<sup>16–19</sup>

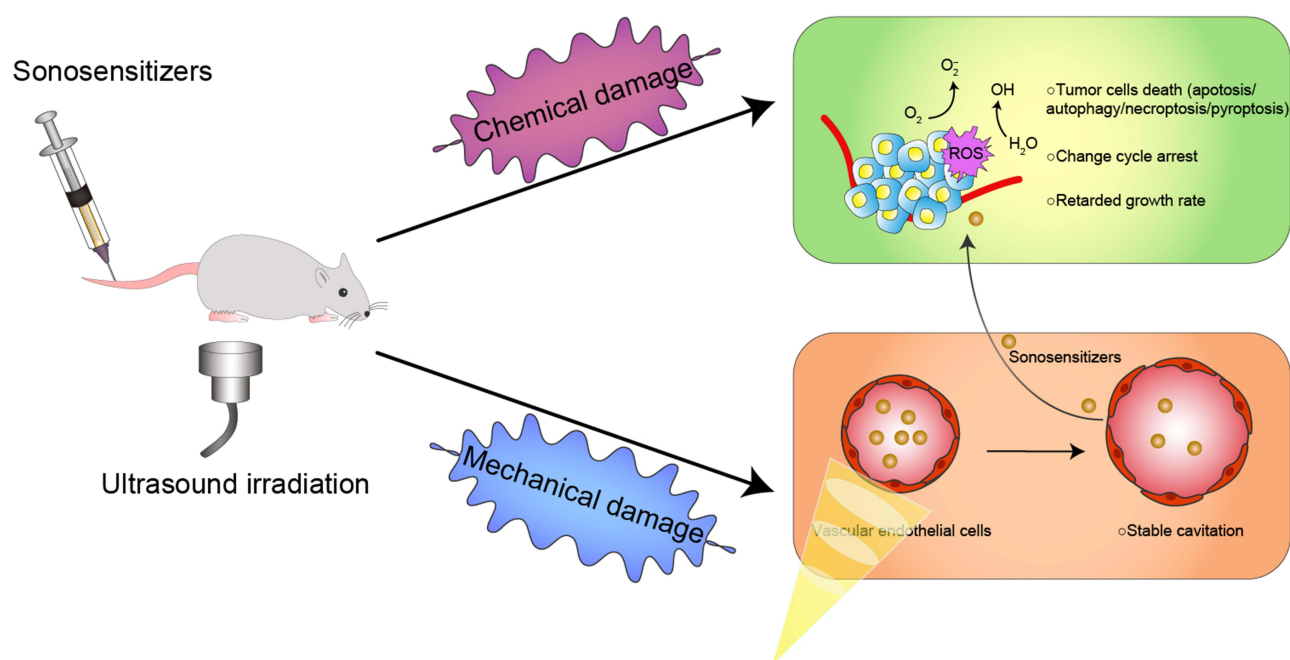


**Figure 1** Schematic illustration of the mechanism of sonodynamic therapy. The stable cavitation induced by ultrasonic irradiation promoted the sonosensitizer to enter the target area from the blood vessel, while the irradiation caused the sonosensitizers to produce ROS to kill tumour cells.

On the other hand, due to the rapid advancement of diagnostic imaging technology, molecular imaging has emerged as a novel diagnostic tool with excellent resolution and sensitivity.<sup>20</sup> Some diagnostic imaging methods, such as photoacoustic (PA) imaging, computed tomography (CT), and magnetic resonance (MR) imaging, have high spatial resolution and penetrate deep into the tissue.<sup>21–23</sup> Therefore, many novel sensitizers developed by researchers combine diagnostic imaging capabilities with treatment capabilities. Nanoparticles can be treated utilizing ultrasound and may also be used to enhance the efficacy of therapy through imaging techniques to observe drug distribution, which can help calculate the best time to start treatment to develop the therapeutic effect.<sup>24,25</sup> As a result, the development of multifunctional drugs that combine tumour targeting, imaging, and therapeutic capabilities is critical for precision oncology.<sup>26–28</sup>

This paper outlines the recent studies using imaging in sonodynamic treatment.

Sonosensitizers are presented in Table 1, summarising the imaging properties of the given article for the reader's ease of "browsing."

## Sonosensitizers with Various Imaging Functions

### Significance of Imaging Applications

The sensitivity, spatial resolution and imaging depth of non-invasive diagnostic imaging methods such as FL imaging, ultrasonography, CT and MR imaging vary.<sup>29</sup> They are all able to detect the location of the disease early. When the sonosensitizer has an imaging function, it may be led by the imaging function to carry out therapy, resulting in the integration of diagnostic and treatment. On the other hand, by utilizing bioimaging in the exact focus of the US and time-dependent tracking of drug retention in the tumour, we can determine the ideal irradiation period during therapy to achieve higher SDT accuracy and limit potential harm surrounding normal tissues.<sup>30</sup> Sonosensitizers with imaging capabilities will be discussed in the following sections.

### MR Imaging

MRI is an imaging paradigm that is commonly used in disease diagnosis and localization with excellent spatial resolution.<sup>31</sup> MRI measures such as longitudinal relaxation (T1), transverse relaxation (T2), and proton density (PD)

**Table I** Imaging Characteristics of the Multifunctional Sonosensitizers

Imaging	Probes	Sonosensitizers	Refs
MR	Ga <sup>3+</sup> (T1) Gd-DTPA-BMA (T1) Mn-TPPS (T1) MnO <sub>2</sub> (T1) PMnC (Mn) (T1) MnTTP (Mn) (T1) MOFs (Fe <sup>3+</sup> ) Fe <sup>3+</sup> (T1) Mn (III) (T1/T2)	OCN-PEG-(Ce6-Gd <sup>3+</sup> )/BNN6, GDHF-ND F3-PLGA@MB/Gd NPs DOX/Mn-TPPS@RBCS GOX-MnO <sub>2</sub> /HMME, AIMP NPs MG@P NPs MnTTP-HSAs UPFB Fe-TiO <sub>2</sub> NDs, Fe-VS <sub>2</sub> NSs Mn (III)-HF <sub>s</sub>	[30,34,35,39–41,119–121,134,150,155]
CT	Au@mSiO <sub>2</sub> AgBiS <sub>2</sub>	GMCDs-FA@CMC ABS-FA	[25,43]
CEUS	PFP PFH FMSNs HMTNPs-SNO RB-MBs mTiO <sub>2</sub>	CPDP NPs, PIO_NPs, OIX_NP, IR780-NDs BBC-HPBS/HMME/PFH, LIP3, OI_NPs, FA-OINPs FMSNs-DOX TPZ/HMTNPs-SNO RB-MBs mTiO <sub>2</sub> @PPYs	[51,60,70,74,130,131,141,143–146,156]
PA	HMPs IR783 PMnC (porphyrin) MnTTP (TTP) HMME VS <sub>2</sub> ICG MB PPY IR780	FHMP NPs Ce6-PTX@IR783 MG@P NPs MnTTP-HSAs IHG@P NPs Fe-VS <sub>2</sub> NSs TPI, PIO_NPs, OI_NPs, OIX_NPs, FA-OINPs F3-PLGA@MB/Gd NPs mTiO <sub>2</sub> @PPYs AIMP NPs, IR780-NDs	[93,94,120,121,124,134,140,141,143–146,150,155,156]
FL	Ag <sub>2</sub> S QDs APHB MOFs (porphyrin) IR780 Rose Bengal ICG	(QD@P) Rs APHB NPs UPFB IHG@P NPs, AIMP NPs, IR780-NDs RB-MBs TPI	[100,101,119,124,131,140,155,156]
IR	AgBiS <sub>2</sub>	ABS-FA	[43]

may identify human tissues. In clinical practice, T1/T2 contrast pictures can be obtained by changing the MRI scanner settings to emphasize or saturate tissue image intensity.<sup>32</sup> The acquired data can identify histology, quantify changes in disease severity, and objectively monitor therapy.<sup>33</sup>

Metal ions have been shown to have MRI imaging capabilities, and sonosensitizers can create regulated therapeutic effects. Based on this function, metal-containing nano-sonosensitizers with sonodynamic therapeutic benefits have been developed extensively.<sup>30</sup> Zhang et al created OCN-PEG-(Ce6-Gd<sup>3+</sup>)/BNN6 nanocomposite by organically combining Ga<sup>3+</sup> with sonosensitive agent e6(Ce6) and loading the N, N'-di-sec-butyl-N, N'-dinitro-1, 4-phenylenediamine (BNN6).<sup>34</sup> The brightness of T1-weighted images was correlated with the Gd<sup>3+</sup> concentration in a 0.5T MRI system. The longitudinal relaxation rate (r1) and transverse relaxation rate (r2) are 89.0 and 103.5 mm<sup>-1</sup>s<sup>-1</sup>, respectively, much higher than the routinely employed gadolinium chelating contrast agent. After injection (4 mg/mL) into mice, MR images of tumour sites increased in brightness at 12 h and 24 h. Sub-5 nm Gd<sup>3+</sup>-hemoporphin framework nanodots (GDHF-NDs) were created by Geng et al as multifunctional therapeutic nanoagents for malignancies.<sup>35</sup> In a 3T MR scanner, the MRI

images of the solution got brighter and brighter as its concentration (0–0.1 mg/mL) increased. After intravenous injection (150 L, 2.0 mg/mL), the signal intensity of tumour tissue increased from  $751.7 \pm 33$  to  $1193.5 \pm 56$  after 3 h and then decreased to  $1118.3 \pm 21$  after 6 h. It was worth mentioning that the size of GDHF-ND was less than 5 nm and belonged to ultrafine nanomaterials (10 nm), which could be successfully filtered through the kidney and contribute to biosafety due to its fast clearance rate.<sup>36–38</sup> This was also supported by the time-dependent biodistribution study in this research. Geng et al created nanomaterials Mn (III) -HMME frameworks (Mn (III) -HFs) with MRI imaging and SDT effect employing Mn (III) ions as metal nodes and hemoporphyrin monomethyl ether (HMME) as sonosensitized ligands.<sup>30</sup> The T1 signal intensity of Mn (III) -HFS/PEG increased with concentration (0–0.2mm), while the T2 signal intensity decreased. In particular, Mn (III) is converted to Mn (II) after interacting with GSH, and Mn (II) ion contains more unpaired electrons, resulting in a slight improvement in T1/T2-weighted MRI image. In CT26 tumour-bearing mice (150 L, 2 mg/mL), the intensity of the T1 signal intensity reached a high of  $2603.1 \pm 250.9$  at 4 h, but the T2 signal intensity dropped from  $2647.2 \pm 269.9$  before injection to  $1696.1 \pm 111.3$  4 h later and  $1905.1 \pm 140.9$  8 h later. Du et al developed a unique nanoparticle DOX/Mn-TPPS@RBCs, an oxygen-producing RBC carrier system for combinatorial sonodynamic and chemotherapy in breast cancer.<sup>39</sup> In vitro investigations using a 3T MRI system revealed a concentration-dependent whitening response for nanomaterials with varied concentrations. The  $r_1$  value was  $18.32 \text{ mm}^{-1}\text{s}^{-1}$ . MR images of tumour-bearing mice (Mn-TPPS: 3.5 mg/kg) demonstrated the strongest signal of 118 a.u. At 12h after injection, the signal lasted for 24h. Zhang et al used glucose oxidase (GOx) and mesoporous  $\text{MnO}_2$  NPs to construct a cascade catalytic nanoplatform GOx- $\text{MnO}_2$ /HMME, which could play a synergistic role in SDT and starvation therapy on breast cancer tumours.<sup>40</sup> After incubating GOx- $\text{MnO}_2$ /HMME solutions with glucose (1 mg/mL) for 1 hour, the was greater in the  $\text{MnO}_2$  NPs group ( $r_1 = 2.88 \text{ mm}^{-1}\text{s}^{-1}$ ) than in the untreated group ( $r_1 = 0.86 \text{ mm}^{-1}\text{s}^{-1}$ ). Subsequently, tumour-bearing mice were injected with nanomaterials ( $[\text{MnO}_2] = 10 \text{ mg/kg}$ ) for 3 h, followed by T1-weighted imaging using a 3.0T clinical scanner, which demonstrated an increased signal at the tumour site. Bai et al's ultra-fine iron-doped titanium dioxide nanodots ( $\text{Fe-TiO}_2$  NDs) conducted combination therapy of CDT and SDT under the dual direction of MR imaging for breast cancer treatment.<sup>41</sup> The  $r_1$  value was estimated to be  $4.71 \text{ mM}^{-1}\text{s}^{-1}$  (Figure 2A). Images and quantitative analysis of the MR signal indicated that the intensity of the T1-weighted MR signal in the tumour region was 1.87 times that of the tumour preinjection (Figure 2B and C).

## CT

CT scans employ computer-processed combinations of multiple X-ray images obtained from various angles to construct an image of the anatomy of the scanned item.<sup>42</sup> CT has been widely used in clinical practice and medical procedures for

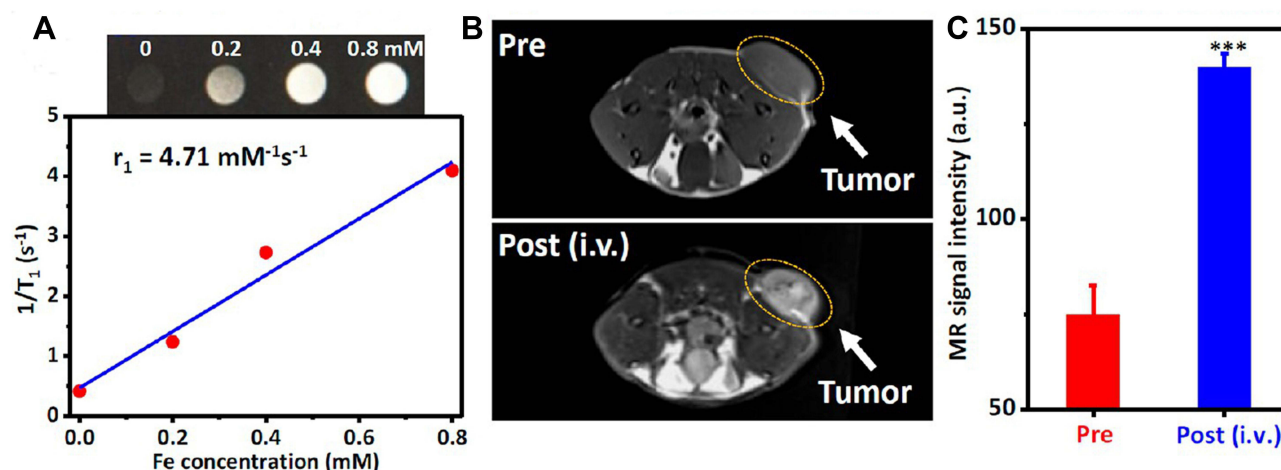


**Figure 2** Imaging properties of  $\text{Fe-TiO}_2$  NDs. (A) MR images of  $\text{Fe-TiO}_2$  solutions with different concentrations and the relative T1 relaxation rates. (B) MR imaging of 4T1 tumour-bearing mice before and after injection of  $\text{Fe-TiO}_2$  NDs for 24 h. (C) Quantification of MR signals from the tumours in (B). Reprinted with permission from Bai S, Yang N, Wang X, et al. Ultrasmall iron-doped titanium oxide nanodots for enhanced sonodynamic and chemodynamic cancer therapy. *ACS Nano*. 2020;14(11):15119–15130. Copyright [2020] American Chemical Society.<sup>41</sup>



its ability to observe what is happening in a patient's body in a non-invasive manner. CT has been used to aid the precise targeting of probes for diagnosis and treatment. Some researchers have conducted studies on the collaboration of probe and CT technology in response to a diverse microenvironment to enhance the tumour microenvironment and achieve tumour therapies.<sup>43</sup>

Zhang et al created enteric-soluble nanoparticle Au@mSiO<sub>2</sub>/Ce6/DOX/SLB-FA@CMC (GMCDS-FA@CMC) capable of pH/ultrasound dual response, CT imaging, and sonodynamic-chemotherapy for colorectal cancer treatment.<sup>25</sup> The gold in mesoporous silicon inside the GMCDS-FA@CMC could be utilized for CT imaging. CT imaging was performed on orthotopic colorectal cancer model mice after oral administration of GMCDS-FA@CMC. The clear CT signal of the tumour was noticed, and the clear signal persisted for 7–9 hours. Findings indicate that GMCDS-FA@CMC has a strong CT imaging impact on guiding sonodynamic chemotherapy.

## CEUS

For many years, CEUS has been routinely utilized to improve imaging of the heart's circulatory system and other organs.<sup>44</sup> CEUS achieves its contrast enhancement effect by the high scattering of ultrasonic pulses by stable microbubbles (MBs) or nanobubbles (NBs) for persistence and echogenicity during intravenous administration.<sup>45,46</sup> MBs and NBs can be used as ultrasound contrast agents and synergistic non-invasive imaging and therapy by using ultrasound to destroy therapeutic genes and drugs encapsulated in the lesion region.<sup>47–50</sup> Consequently, MBs and NBs have a promising future as integrated diagnostic and treatment providers.

Zhang et al recommended using all-in-one nanoparticles (CPDP NPs) to construct a diagnosis and treatment system for breast cancer based on SDT-oriented collaborative therapy combined with chemotherapy and US imaging.<sup>51</sup> Acoustic nanodroplets with a liquid core can be transformed to MBs via acoustic droplet vaporization (ADV) when exposed to US irradiation.<sup>52,53</sup> Additionally, ADV-generated bubbles (ADV-Bs) may have the same properties as microbubbles (MBs).<sup>54,55</sup> The acoustic impedance values of perfluorobutane (PFP) are similar to those of adjacent tissues, so liquid PFP droplets must evaporate into bubbles to become effective US contrast agents.<sup>56,57</sup> The nanodroplet of PFP has a strong phase transition capacity and can go from liquid to gas phase by mediating ADV.<sup>53,58,59</sup> Using a LIFU transducer (50% duty cycle, 1–2 W/cm<sup>2</sup>, 1 s pulse) to irradiate 1 mg/mL emulsion, it was found that 2D and CEUS images were most significant when LIFU intensity reached 2 W/cm<sup>2</sup> and duration was 120 seconds (Figure 3A). In vivo, LIFU irradiation strengthened the images of tumours in mice (Figure 3B). The images' findings were consistent with the trend of data obtained from quantitative analysis (Figure 3C and D). Ho et al developed superhydrophobic mesoporous silica nanoparticles (FMSNs-DOX) loaded with the antitumor medication doxorubicin to treat prostate cancer in their investigation.<sup>60</sup> The hydrophobic surface of mesoporous silica nanoparticles (MSNs) was modified to enhance the concentration of air nanoparticles (NBs) at the interface between the water and the hydrophobic MSNs surface in the previous research.<sup>61,62</sup> These interfacial nanobubbles (INBs) are confined in the cavities supplied by the mesopores of hydrophobic MSNs, allowing them to be employed as nanoscale ultrasonic contrast agents.<sup>61,63–66</sup> Ho et al used perfluorodecyltriethoxysilane (PFDTs) with moderate surface energy and superhydrophobicity as the surface coating of MSNs to make MSNs superhydrophobic in order to improve image contrast by enhancing INB accumulation.<sup>67–69</sup> Analysis of mouse tumours revealed that INBs could be repeated and cavitated from day 1 to day 9 to generate significant contrast enhancement within the tumour. The quantitative findings revealed that the US imaging was steady (3.84 ± 0.47 dB) from day 1 to day 9 and declined with time after day 9. Zhang et al investigated a nanosystem (BBC-HPBS/HMME/PFH) for breast cancer that achieved precision drug administration guided by US imaging and local sonodynamic treatment.<sup>70</sup> Like PFH, PFH was a phase change material that could be converted from liquid to gas to become a US contrast agent when the pressure at the tumour tissue was decreased to the vaporization pressure threshold by an external input of energy.<sup>71–73</sup> In vitro, the aqueous dispersion of RBC-HPBs/HMME/PFH was irradiated with ultrasound (3 MHz, 5.0 W/cm<sup>2</sup>, 30s). Furthermore, the images exhibited concentration-dependent ultrasonic signal amplification. Then, RBC-HPBs/HMME/PFH (5 mg/kg) were administered intravenously into tumour-bearing mice, followed by ultrasonic irradiation (3 MHz, 5.0 W/cm<sup>2</sup>, 30s). A distinct US signal was discovered, and the signal was most outstanding at 8h. Feng et al reported the TPZ/ HMTNPs-SNO therapeutic agent delivery system, which is made by combining tirapazamine (TPZ) with S-nitrosothiol (R-SNO) modified hollow mesoporous titanium dioxide nanoparticles

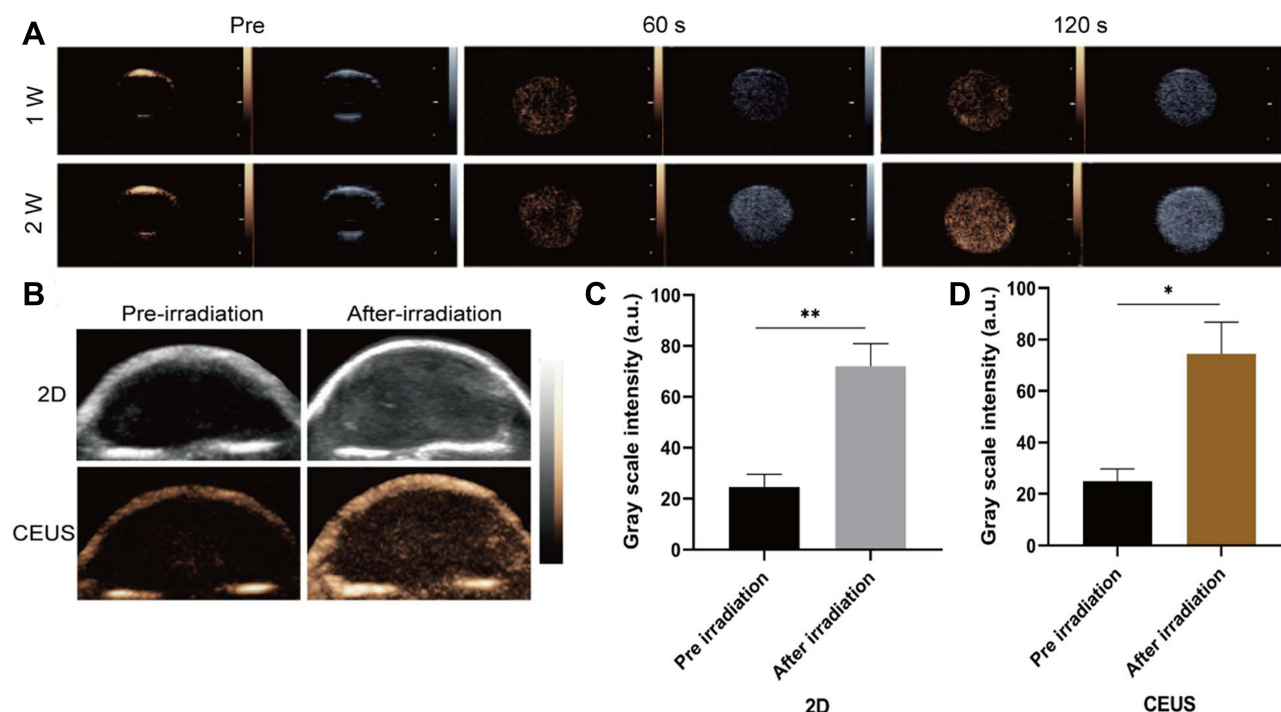


**Figure 3** Imaging properties of CPDP NPs. **(A)** Ultrasound images of 2D and CEUS under different LIFU intensities and duration times. **(B)** 2D and CEUS images with and without LIFU irradiation. **(C)** The corresponding grayscale intensity (\*\* $p < 0.01$ , \* $p < 0.05$ ,  $n = 3$ ). After the H&E, PCNA, and TUNEL staining, the proliferate rate of PCNA in CPDP NPs + LIFU group was only 20.50%. The TUNEL results indicated CPDP NPs + LIFU group exhibited an obvious apoptosis index of 72.86%. Reproduced from Zhang Q, Wang W, Shen H, Tao H, Wu Y, Ma L, Yang G, Chang R, Wang J, Zhang H, Wang C, Zhang F, Qi J, Mi C. Low-Intensity Focused Ultrasound-Augmented Multifunctional Nanoparticles for Integrating Ultrasound Imaging and Synergistic Therapy of Metastatic Breast Cancer. *Nanoscale Res Lett.* 2021;16(1):73. To view a copy of this licence, visit <https://creativecommons.org/licenses/by/4.0/>.<sup>51</sup>

(HMTNPs).<sup>74</sup> Here, Feng et al applied R-SNO, a ROS-sensitized NO donor, to the surface of HMTNPs. Following US activation of HMTNPs to form ROS, the -SNO group would interact with ROS and trigger S-N bond homolysis to release NO.<sup>75</sup> The released NO would exhibit blistering behaviour, thus acting as a US contrast enhancer. In vitro, US images of HMTNPs-SNO after US irradiation (1 W/cm<sup>2</sup>) indicated that the improvement of acoustic contrast was consistent with the increase in NO yield data. In vivo, the HMTNPs-SNO group (20 mg/kg) demonstrated elevated spots at the tumour location following US stimulation (1 W/cm<sup>2</sup>) and increased ultrasonic signal over time.

## Optical Imaging

PA and FL imaging are non-invasive optical imaging techniques.<sup>76</sup> PA imaging is a new hybrid imaging method based on the PA effect.<sup>77</sup> By irradiating endogenous chromophores and exogenous contrast agents with near-infrared (NIR) light at 650–1200 nm, the photon energy is converted into sonic pressure waves to achieve deep tissue penetration of non-ionizing imaging technology that provides high contrast depth imaging and molecular imaging.<sup>59,78,79</sup> Therefore, PA imaging promises to provide practical information about biological tissues, such as vascular networks and oxygenation status in the tumour region.<sup>80,81</sup> Fluorescence imaging is also an exciting diagnostic technique. NIR irradiation or the physiological milieu of a biological condition can activate fluorescent probes, resulting in light emission imaging.<sup>82,83</sup> FL imaging allows for real-time monitoring of imaging probe dispersion throughout the body, including malignancies.<sup>84–88</sup>

Melanin nanoparticles (MNPs) produced from natural biopolymers are excellent contrast agents for PA imaging because of their high light absorption.<sup>89–92</sup> Huang et al designed and synthesized FA-HMME-MNPs-PLGA nanoparticles with core/shell structure utilizing MNPs-linked aromatic structure, and the imaging capacity of MNPs was used to improve the PA image-guided SDT.<sup>93</sup> PA images of FHMP NPs in vitro indicated that they performed best under stimulation at 700 nm. In MDA-MB-231 tumour-bearing mice, the PA signal in the tumour region reached a peak at 2 h after injection of FHMP NPs (200  $\mu$ L, 10 mg/mL). Dong et al assembled nanoscale sonosensitizer Ce6-PTX@IR783

by merging two organic dyes (Ce6 and IR783) with the anticancer agent paclitaxel (PTX).<sup>94</sup> IR783 is a gorgeous hydrophilic heptamethine cyanine dye with excellent optical imaging and tumour targeting properties.<sup>95–97</sup> Ce6-PTX@IR783 reaches its peak PA value at 795 nm. There was a linear relationship between the PA value and the concentration of Ce6-PTX@IR783. After intravenous injection into 4T1 tumour-bearing mice, the PA value peaked at 7 h.

Since Ag<sub>2</sub>S quantum dots (QD) have a tiny bandgap (0.9 eV), they emit light in the near-infrared (NIR).<sup>98</sup> Additionally, Ag<sub>2</sub>S QDs, such as their broad absorbance-narrow emission profile, adjustable emission wavelength, and extended luminescence lifetime, make them excellent for FL imaging in biological tissues.<sup>99</sup> Li et al modified Ag<sub>2</sub>S QDs with Pluronic F-127 and coated them with RBC vesicles to form biomimetic agent (QD@P) Rs for enzyme-enhanced SDT.<sup>100</sup> The FL signal at the tumour sites peaked at 6–9 h after (QD@P) Rs were injected into C26 xenograft mice, then a faint FL signal was obtained 24 h later. Zhang et al constructed a hypocrellin derivative sonosensitizer (APHB NPs) to improve the depth of tumour therapy.<sup>101</sup> Hypocrellins is a water-soluble metabolite produced by the traditional Chinese medicine fungus *Hypocrella Bambusae*, with high singlet oxygen production and broad spectrum absorption in the NIR.<sup>102,103</sup> In this experiment, the modification of hypocrellin B by 1, 2-diaminopropane made the obtained APHB possess excellent FL imaging ability and water solubility (Figure 4A). After 638 nm laser irradiation of 4T1 tumour mice, intratumoral FL reached a plateau 7 h after injection of APHB NPs, and diminished substantially 48 h later (Figure 4B and C). Ex Vitro FL images indicated that FL signals in tumors were remarkably higher than in other tissues (Figure 4D and E).

## Multimodal Imaging

### Advantages of Multimodal Imaging

It is well-known that multimode imaging supplies more reliable physiological information for the early detection and therapy of cancer by incorporating the advantages of individual diagnostic imaging.<sup>104</sup> Due to equipment limitations, the data provided by single-mode imaging is often short of the high precision and reliability required for diagnosing, surgical guidance and prognostic assessment.<sup>105</sup> Ultrasound imaging, for example, is hindered by weak penetration in gas. MRI is much less sensitive than other types of imaging. Soft tissue contrast is frequently a limitation of CT imaging. Due to the scattering of solid light in cells or tissues, the resolution of fluorescence imaging diminishes significantly as the imaging depth increases, limiting the technique's practical imaging depth. Many multimodal imaging materials based on nanoparticles have been produced to date in order to achieve better imaging and early treatment.<sup>29,106–109</sup>

### Dual-Mode Imaging

Porphyrins could generate fluorescence in the red wavelength part of the spectrum after UV or violet stimulation, used for PA and FL imaging.<sup>110,111</sup> Moreover, nanoparticles constituted of varying metal ions (Mn and Cu ions) could redox with glutathione (GSH), thus releasing metal ions to induce MRI.<sup>112–115</sup> When porphyrin was synthesized with metal to form the metal-porphyrin complex, it would become a dual mode contrast agent. Such potent nanoparticles have been used to design nanoparticles with specific therapeutic properties.<sup>116–118</sup> Wang et al created UPFB nanocomposites with Janus nanostructures made of UCNP and porphyrin-based MOFs [PCN-224 (Fe)] to achieve direct photodynamic and sonodynamic co-therapy.<sup>119</sup> The FL signal in the tumour started to arise at 1 h after intravenous infusion, with the brightest signal released at 4 h (Figure 5A and B). Then the intensity progressively diminished 12 h later, but the intensity in the liver and kidney climbed (Figure 5C). The  $r_2$  of UPFB in the GSH solution was  $55.17 \text{ mM}^{-1}\text{s}^{-1}$ . This implied that UPFB can react with GSH to convert Fe<sup>3+</sup> into T2-weighted MRI contrast agent Fe<sup>2+</sup>. In addition, after the addition of H<sub>2</sub>O<sub>2</sub> and GSH,  $r_2$  was  $81.06 \text{ mM}^{-1}\text{s}^{-1}$ , which was because neutral conditions facilitated the transformation of catalase-like Fe<sup>3+</sup> into Fe<sup>2+</sup>. The 1.2T MR scanner showed that the tumour site in the UPFB-treated group darkened over time compared to the mice injected with UPF (Figure 5D). Wang et al created MG@P NPs for synergistic starvation treatment and SDT by encapsulating GOx and 5, 10, 15, 20-tetrakis (4-chlorophenyl) porphyrin) Cl (denoted PMnCl) in poly (lactic-co-glycolic) acid (PLGA) NPs.<sup>120</sup> The increase of T1-weighted and PA signal intensity was positively correlated with MG@P NPs concentration. The semi-quantitative T1 signal intensity reached the peak at 24 h after injection in 4T1 tumour-bearing mice. The peak of the PA signal occurred around 24h, which corresponded to the strongest signal in MR imaging. Similarly, Ma et al designed HSA-wrapped metal-porphyrin complex (MnTTP-HSAs) by utilizing Mn ion and 4-methylphenylporphyrin (TTP) ligand, which

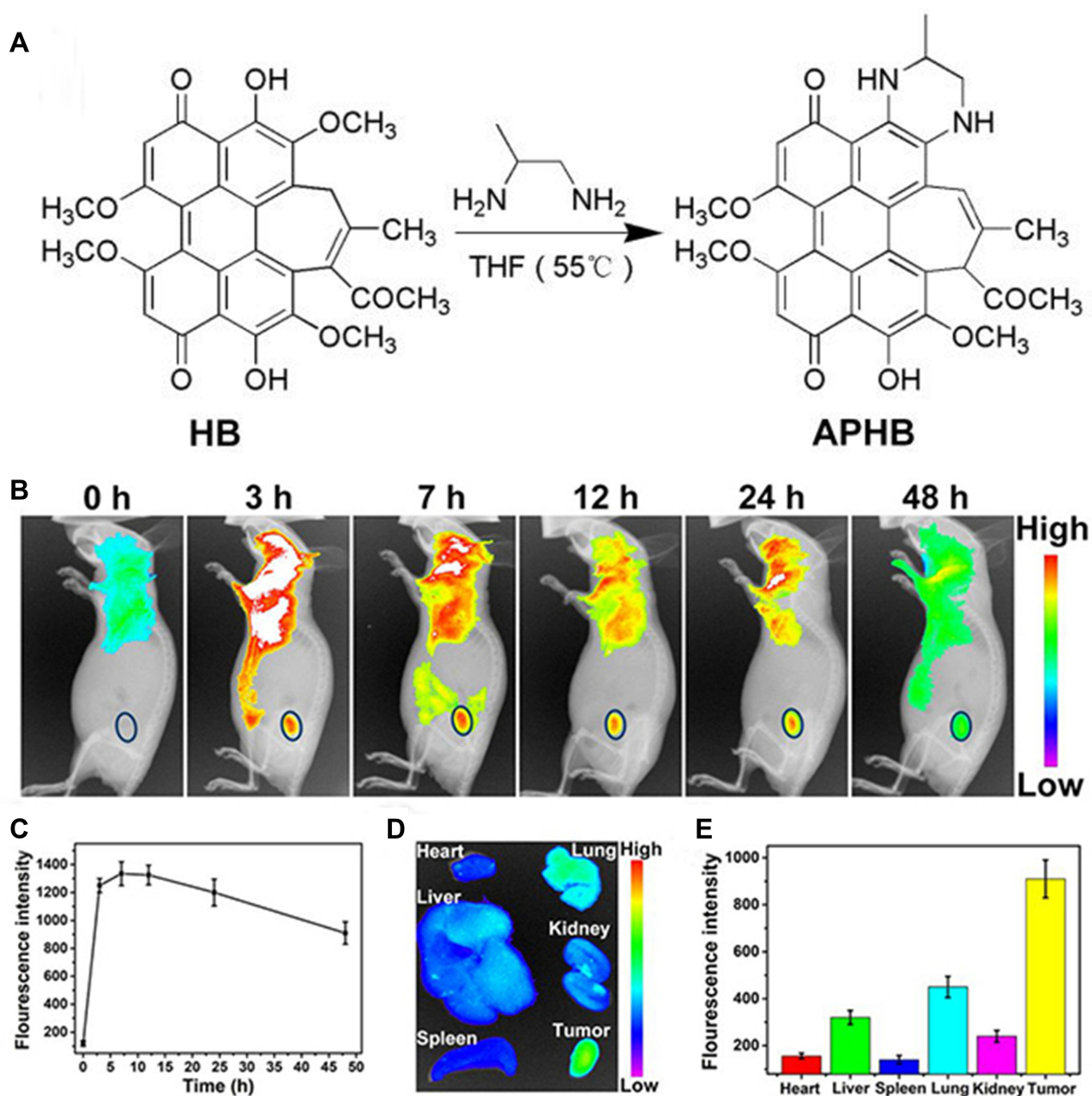


**Figure 4** Synthesis and imaging properties of APHB NPs. **(A)** The synthetic route of APHB. **(B)** FL images of the mice and **(C)** FL intensities of the tumour at different time points post-injection of APHB NPs. Ex vivo **(D)** FL images and **(E)** FL intensities of major organs and tumours at 48 h post-injection of APHB NPs. Approximately 90% cell death is found at the concentration of 100  $\mu\text{g/mL}$  under ultrasound stimulation (0.6 V/cm, 60s).

**Notes:** Reprinted with permission from Zheng X, Liu W, Ge J, et al. Biodegradable natural product-based nanoparticles for near-infrared fluorescence imaging-guided sonodynamic therapy. *ACS Appl Mater Interfaces*. 2019;11(20):18178–18185. Copyright 2019 American Chemical Society.<sup>101</sup>

can conduct MR/PA image-guided SDT in deep tumour tissues.<sup>121</sup> The image findings are shown in Table 1. Dong et al created AgBiS<sub>2</sub>@DSPE-PEG2000-FA(ABS-FA), targeted multifunctional hydrophilic nanomicelles and used them to treat breast cancer.<sup>43</sup> Ternary alloy silver bismuth sulfide (AgBiS<sub>2</sub>, ABS) nanodots exhibited excellent X-ray attenuation, high near-infrared absorption, and photothermal conversion efficiency, making them an ideal CT/IR bimodal imaging agent (Figure 6A and B).<sup>122,123</sup> After the injection of ABS-FA (300  $\mu\text{L}$ , 5 mg/mL), CT signals appeared at the tumour site and increased steadily, reaching a peak at 6–12 h (Figure 6C). Furthermore, in vivo low power (0.35W/cm<sup>2</sup>) infrared thermal imaging results were consistent with CT, with the thermal signal at 2 h and the maximum thermal signal at 10 h (Figure 6D).



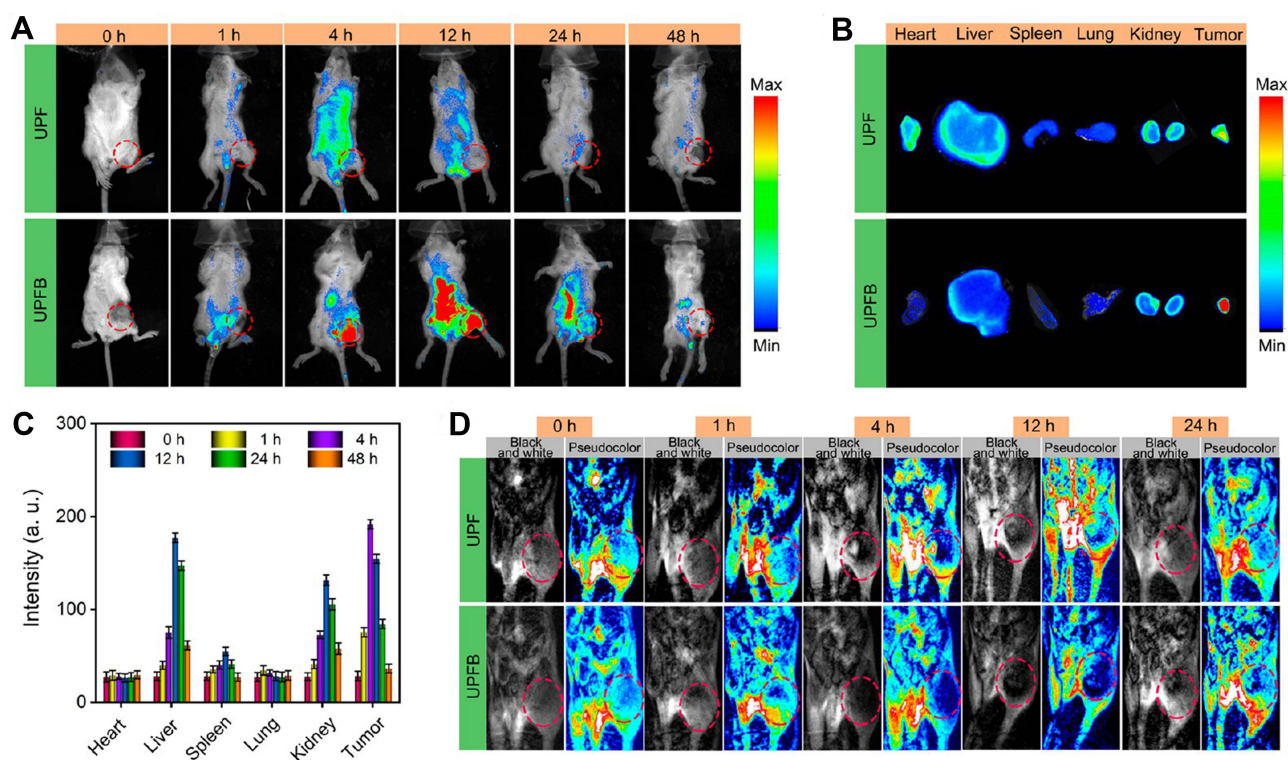


**Figure 5** Imaging properties of UPFB. (A) FL images of U14-tumour-bearing mice taken after i.v. injection of UPF and UPFB. (B) Ex vivo fluorescence images of major organs and tumours at 4 h post-injection with UPF and UPFB. (C) FL intensity of the major organs and tumours at different times. (D) T2-MRI of a tumour-bearing mouse with i.v. injection of UPF or UPFB at different time intervals. The tumour site was labelled with a red ellipse. The high contents of UPFB without DMTU upon irradiation with the 808 nm laser and US exhibited the lowest cell viability rates (16.7%).

**Notes:** Reprinted with permission from Wang Z, Liu B, Sun Q, et al. Upconverted metal-organic framework janus architecture for near-infrared and ultrasound co-enhanced high performance tumor therapy. *ACS Nano*. 2021. Copyright [2021] American Chemical Society.<sup>119</sup>

Zhang et al used PLGA as a carrier to add IR780 and HMME to the shell and wrapped GOx to synthesize IHG@P NPs with mitochondrial targeted synergistic SDT and starvation therapy effects.<sup>124</sup> Previous research has demonstrated that HMME can be utilized in PA imaging of malignancies.<sup>125,126</sup> At the same time, IR780 has a significant near-infrared absorption peak and generates high-intensity fluorescence in the 807–823 nm wavelength region, making it suitable for PA and FL imaging applications.<sup>127–129</sup> In vitro, PA imaging of the IHG@P solution determined an optimal excitation wavelength of 800 nm. At 24 h after intravenous administration of IHG@P NPs (5 mg/mL, 200  $\mu$ L) to 4T1 xenograft mice, PA signal intensity in the tumour region increased 3.02 times before injection. For FL imaging, the signal could be observed at the tumour sites 1h after injection and reached a peak at 24h. Zhao et al created the LIP3 liposome nanosystem, which consists of a lipid bilayer of HMME as the shell, PFH and water-soluble prodrug banoxantrone (AQ4N) as the core.<sup>130</sup> CEUS imaging revealed that when AI was 6 W/cm<sup>2</sup>, the echo signal attained its maximum value after 3 min. In PA imaging, the PA signal increased with increasing concentration, and the linear correlation coefficient between them was  $R = 0.992$ . Hou et al constructed an amphiphilic Rose Bengal (ARB) and encapsulated it in fluorine gas to create a new sonosensitizer (RB-MBs).<sup>131</sup> The fluorescent and photosensitive Bengal Rose was coupled with dihexalkylamine via a stable amine link to generate the ARB, employed as a sonosensitizer and FL imaging agent.<sup>132,133</sup> Simultaneously, CEUS would be performed using MBs generated by fluorinated gas encapsulated by ARB. There was a distinct ultrasonic signal when the concentration of RB-MBs reached  $6.2 \times 10^{-6}$  MBs/mL in vitro. In mice with HT-29 tumours, an instant increase in US signal was seen at the tumour site and lasted more than 4 minutes. Furthermore, clear fluorescence signals were observed at the tumour site using 523nm and 610nm excitation wavelength filters. Lei et al reported iron-doped vanadium disulfide nanosheets (Fe-VS<sub>2</sub> NSs) for sonodynamic/chemodynamic combination therapy.<sup>134</sup> Vanadium disulfide (VS<sub>2</sub>) has demonstrated promising MR/PA multimodal imaging.<sup>135</sup> Simultaneously, metal doping in TMDC can optimize its physical properties, allowing them to adapt to a wider range of applications.<sup>136</sup> PA images of 4T1 xenograft mice after injection of FE-VS<sub>2</sub>-PEG NSs (7.5 mg/kg)



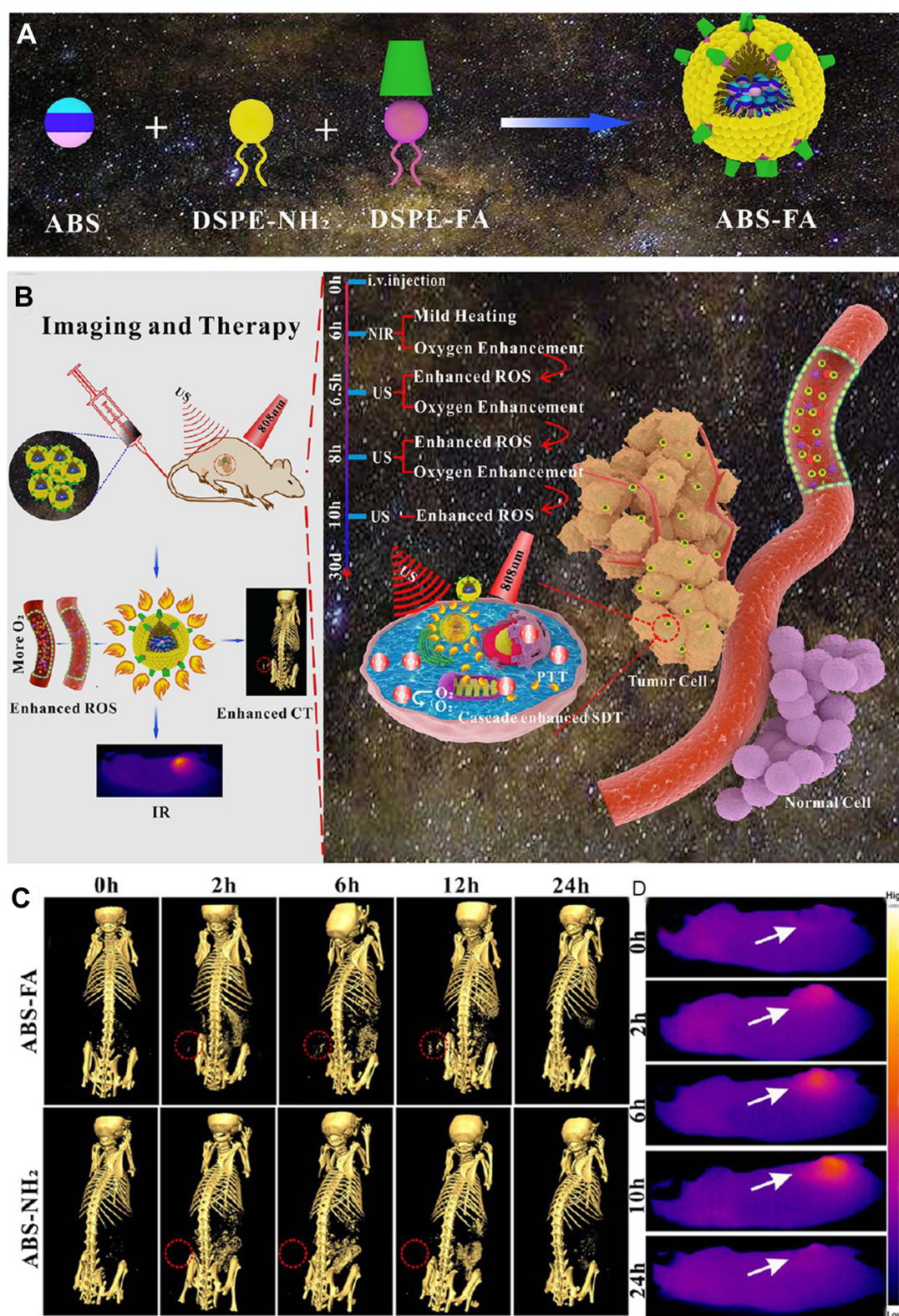


**Figure 6** Synthesis and imaging properties of ABS-FA. **(A)** Schematic illustration for the synthesis of ABS-FA. **(B)** surgical navigation during tumour treatment. **(C)** CT imaging of HeLa tumour-bearing mice after injection of ABS-FA and ABS; red dotted circle: the tumour site. **(D)** Low-power (0.35 W/cm<sup>2</sup>) infrared thermal imaging of tumour-bearing mice at different time points. When HeLa cells underwent NIR irradiation and ultrasound treatment simultaneously, the survival rate when cultivated with ABS-FA was only 8.99%.

**Notes:** Reprinted with permission from Cheng K, Zhang RY, Yang XQ, et al. One-for-all nanoplatform for synergistic mild cascade-potential ultrasound therapy induced with targeting imaging-guided photothermal therapy. *ACS Appl Mater Interfaces*. 2020;12(36):40052–40066. Copyright [2020] American Chemical Society.<sup>43</sup>

showed an obvious PA signal in the tumour area. The  $r1$  was  $19.968 \text{ mm}^{-1}\text{s}^{-1}$ , which was greater than the  $r1$  of the VSx nanoplatfrom studied in the past, indicating that the addition of  $\text{Fe}^{3+}$  might enhance the MRI ability of the V element. According to the PA imaging results, the intensity of the MR signal in mice rose to 2.04 times that before injection. Indocyanine green (ICG) has been verified to have moderate fluorescence quantum yield and absorption in the NIR, which could be used in optical (PA/FL) imaging.<sup>137–139</sup> Because it also functions as a sonosensitizer, it is frequently employed to build novel multifunctional sonosensitive agents. Yang et al assembled the sonosensitizer ICG and TPGS-PEM prodrug (D- $\alpha$ -tocopheryl polyethylene 1000 succinate (TPGS) modified by pemetrexed (PEM)) into dual-mode imaging and active targeting TPGS-PEM-ICG nanoplatfrom (TPI).<sup>140</sup> The FL signal of HeLa tumour-bearing mice was the highest at 6 h and lasted until 24 h after TPI injection through the tail vein. The peak PA signal in the tumour area reached the peak 6 h after injection. Chen et al prepared oxygen-carrying PLGA nanoparticles (PIO\_NPs) using PLGA as the shell loaded of ICG and PTX to encapsulate PFP and oxygen.<sup>141</sup> Following laser irradiation, ICG wrapped in a PFP droplet will generate an immediate temperature rise, leading to evaporation of the PFP droplet into the gas phase and subsequently producing US and PA imaging functions. Meanwhile, The thermal tissue expansion caused by the temperature rise of ICG will generate an ultrasonic pressure wave, which magnifies the US/PA signal.<sup>77,142</sup> In vivo, the intensity of the PA signal in the tumour was heightened at 2 h, peaked at 6h and lasted until 12h. So, the optimal imaging time was 6 h. At this time, the average PA value (a.u.) increased from  $0.26 \pm 0.02$  to  $0.37 \pm 0.03$  after near-infrared irradiation ( $1.5 \text{ W/cm}^2$ , 5 min). The EI of B-mode was also increased substantially. Analogously, Xie et al and Zheng et al created OI\_NPs and OIX\_NPs that were similar to PIO\_NPs in that they encapsulated PFP with PLGA and loaded ICG, and they used the imaging features of the ICG and PFP bubbles to develop the PA/US imaging performance of sonosensitive nanoparticles.<sup>143,144</sup> Liu et al loaded ICG and folic acid target molecules into the shell using lipids as carriers and encapsulated oxygen-carrying PFH to synthesize nanoparticles (FA-OINPs) to achieve dual-mode imaging monitoring for ovarian cancer treatment.<sup>145</sup> All groups were irradiated with a  $1.5 \text{ W/cm}^2$  laser for 5 min. In vitro, the EI of CEUS increased to 22.49 times that before the irradiation. The EI of B-mode increased from  $(33.05 \pm 2.78) \text{ a.u.}$  to  $(83.09 \pm 12.36) \text{ a.u.}$  Consistently, the PA values increased from  $(0.31 \pm 0.02) \text{ a.u.}$  to  $(0.72 \pm 0.08) \text{ a.u.}$  In vivo, the optimal imaging time for US and PA imaging was 6 h after injection ( $64 \mu\text{g/mL}$  of ICG,  $200 \mu\text{L}$ ). He et al synthesized multifunctional nanocomposites ( $\text{mTiO}_2@\text{PPYs}$ ) by combining mesoporous  $\text{TiO}_2$  nanoparticles ( $\text{mTiO}_2\text{s}$ ) with photothermal polypyrrole (PPY), which has a synergistic therapeutic effect on tumours.<sup>146</sup> In this research, the author discovered that pure  $\text{mTiO}_2$  could play the role of US imaging in vivo and in vitro, which was not found in other articles. The outer PPY layer is a typical conjugated polymer with a larger length than polycyclic aromatic compounds (such as porphyrins), which leads to an increase in absorption coefficient and transfer of absorption to higher absorption wavelengths, resulting in better PA imaging performance.<sup>147–149</sup> In vivo, the intensity of the US signal increases with increasing concentration of  $\text{mTiO}_2@\text{PPY}$ . The US and PA signals were also detected in vivo in the tumour region of tumour-bearing mice in the  $\text{mTiO}_2@\text{PPY}$  group. Li et al designed a nanoplatfrom ( $\text{F3-PLGA}@\text{MB/Gd NPs}$ ) that effectively coloureds sonosensitizer (methylene blue, MB) and Gd-DTPA-BMA, integrating dual-mode imaging (PA and MRI) with dual-mode treatment (SDT and HIFU ablation).<sup>150</sup> Methylene blue (MB) is a hydrophilic phenothiazine derivative that may be employed as a sonosensitizer and a PA contrast agent.<sup>151–154</sup> At the same time, Gd-DTPA-BMA as an MRI contrast agent and MB work together to improve imaging ability. With the increase in concentration, the intensity of the T1 signal and PA signal became clearer at a wavelength of 700 nm. High-resolution PA and MR tumour images appeared at 6 h after injection of  $\text{F3-PLGA}@\text{MB/Gd NP}$  solution ( $0.2 \text{ mL}$ ,  $10 \text{ mg/mL}$ ) in MDA-MB-231 tumour mice.

### Triple Mode Imaging

Liu et al constructed a nanoparticle ( $\text{ANG-IR780-MnO}_2\text{-PLGA}$ , AIMP) with multimode (PA/FL/MR) imaging capability utilizing IR780 and  $\text{MnO}_2$ .<sup>155</sup> In vitro, the FL, PA signal and  $1/T1$  value were concentration-dependent. The  $r1$  was 6.119 under simulated TEM settings (pH 6.5, 2 mM GSH,  $100 \mu\text{M H}_2\text{O}_2$ ), which was considerably higher than the pH 7.4 (physiological environment) group, indicating that AIMP NPs may be employed as TME stimuli-responsive T1 MRI contrast agents. After injection of AIMP NPs ( $2 \text{ mg/mL}$ ,  $300 \mu\text{L}$ ) into U87 MG xenograft mice through the vein, FL signalling at the tumour site peaked at 4 h and kept high until 24 h. After administration, the changing trend of the PA signal was consistent with FL imaging data. However, the maximum strength of the MR signal arrived later, at 6h. However, due to the hyperoxic level of the tumor site, 6h may be the best time for LIFU irradiation. Zhang et al described



the construction of nanodroplets (IR780-NDs) utilizing IR780 and PFP for multimode (FL/PA/US) imaging-guided SDT.<sup>156</sup> It was observed under an optical microscope that a large amount of IR780-NDs was transformed into MB with an average size of about 2  $\mu\text{m}$  after 3 min of irradiation at 2.4  $\text{W}/\text{cm}^2$ . A significant increase in US intensity was also observed (Figure 7A and B). Under irradiation with a 780 nm laser, the PA signal expanded linearly with the IR780-NDs concentration (Figure 7C). In 4T1 tumour-bearing mice, the US signal in CEUS mode was bright 24 h after injection (Figure 7D). Furthermore, the quantitative biodistribution analysis showed that the EI was considerably higher after injection than before (Figure 7E). Meanwhile, the PA signal peaked at about 24 h after injection (Figure 7F and G). FL

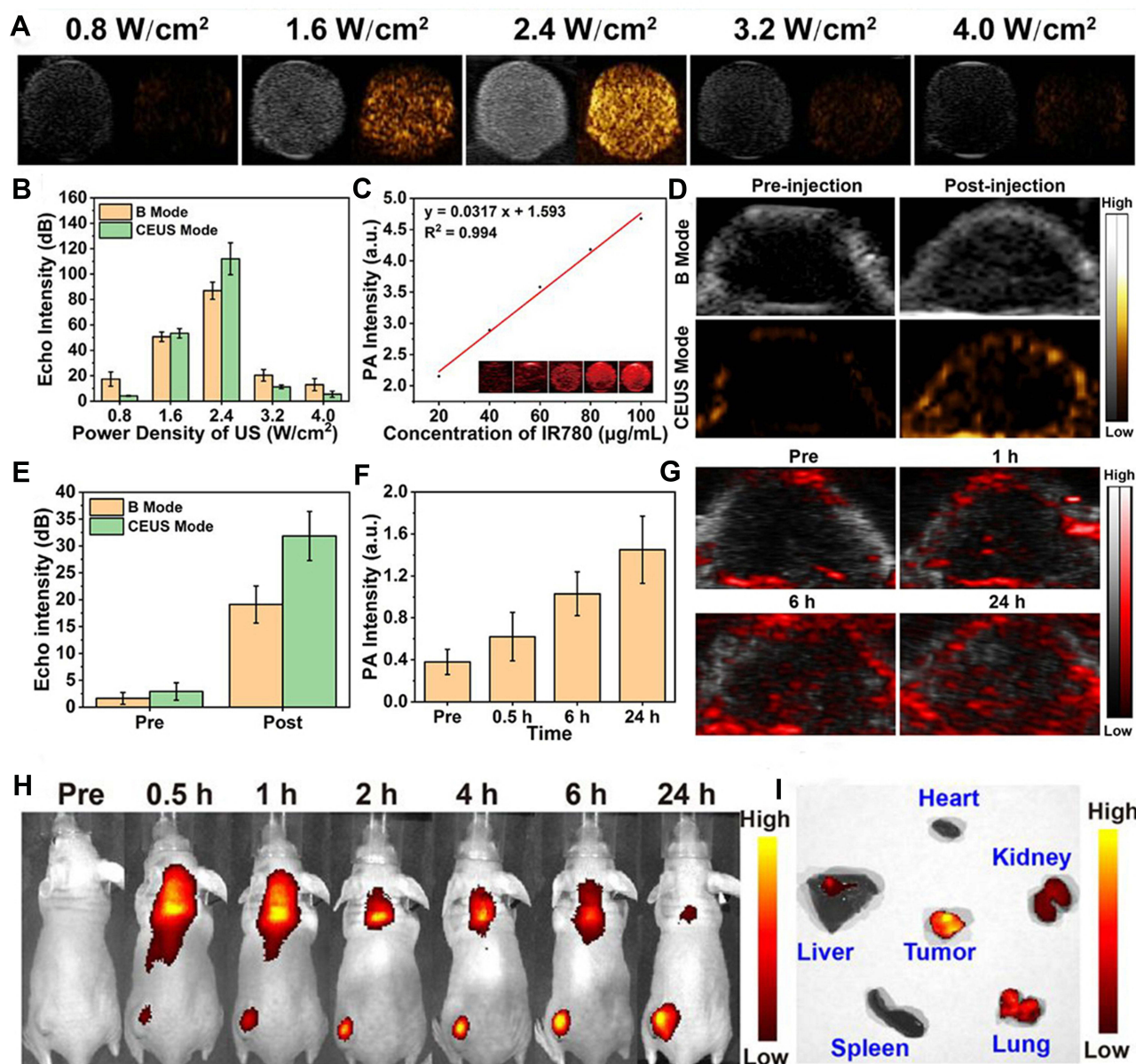


**Figure 7** Imaging properties of IR780-NDs. (A) The US images (CEUS and B-mode) and corresponding quantitative analysis (B) of the echo intensities. (C) PA images and PA values at different concentrations. (D) CEUS and B-mode imaging before and after US irradiation. (E) Corresponding echo intensities of tumours. (F) Changes in PA signal intensities and images (G) at the tumour regions at the corresponding time points. (H) FL images of tumours in 4T1 tumour-bearing mice at different time points. (I) Ex vivo FL images of major organs and tumours dissected from mice 24 h post-injection. 91.52% of cells died in the IHG@P group. The lowest tumor volume was recorded in the IHG@P + US group (1.94-fold increase).

**Notes:** Reprinted with permission from Zhang L, Yi H, Song J, et al. Mitochondria-targeted and ultrasound-activated nanodroplets for enhanced deep-penetration sonodynamic cancer therapy. *ACS Appl Mater Interfaces*. 2019;11(9):9355–9366. Copyright [2019] American Chemical Society.<sup>156</sup>

signal was prominent at 0.5–24 h (Figure 7H). Ex Vitro FL images showed that FL signals of tumours were more significant than in other organs (Figure 7I).

### Reflection of Multimodal Imaging Nanoparticles

Hybrid imaging approaches provide the benefits of high temporal and spatial sensitivity and anatomical and functional information by integrating single imaging modes. Scan time and dosage can be lowered by injecting multimode probes, and the enhanced imaging signal can be used for diagnosis, localization, and therapy guiding. It should be noted that significant differences in sensitivity between different techniques mean that multimode optimized seekers require a large number of low-sensitivity seekers to meet the ideal probe concentration for each imaging mode or multimode probes that can overcome sensitivity differences need to be designed to achieve synchronous data acquisition. The crucial question is whether the properties of each mode in the multimode nanoparticle are comparable sufficiently to those of the single-mode nanoparticle that each portion of the combined injection may offer the same information as the corresponding single probe. This challenge cannot be overcome by solely raising probe concentrations for different forms of imaging or by integrating various types of imaging probes. In a nutshell, the fusing of nanoparticles with varied functionalities without compromising the individual efficiency of each function is a problem to resolve when establishing novel integrated diagnostic and therapeutic vectors. On this basis, we briefly summarized the main synthesis strategies of sonosensitizers in Table 2, which can provide new ideas and guidance for the development of sonosensitizers in the future.

### Sonosensitizers Beyond Imaging

With the expansion of basic research, people are paying more and more attention to the genetic level of treatment and monitoring methods to find a cure for cancer.<sup>157</sup> The delivery function of sonosensitizers could transport therapeutic genes to the target to achieve gene therapy for tumours. Multiple studies have supported that multifunctional sonosensitizers could alter gene expression in cancer and immune-related cells and revealed therapeutic target genes in various signaling pathways by the data analysis.<sup>158–161</sup> For example, Wu et al designed IR820@NCP using RAS inhibitor Farnesyl-Thiosalicylic acid (FTS) to demonstrate that SDT combined with FTS predominantly achieved anti-tumour effects by inhibiting endothelial cells and stimulating host immunity.<sup>160</sup> In Chen et al's research on the treatment of liver cancer by RSL3@O2-ICG NBs, essential genes were identified to affect the sensitivity of hepatocellular carcinoma to iron death.<sup>158</sup> In addition to molecular imaging techniques, such gene and protein level monitoring could be achieved by reporter imaging techniques that combined reporter proteins with corresponding imaging probes.<sup>162</sup> Because the reporter

**Table 2** Synthesis Strategies of Sonosensitizers

Synthesis Strategies	Sonosensitizers	Refs
Self-assembly	GdHF-NDs, Mn (III)-HFs, Ce6-PTX@IR783, APHB NPs, TPI, ABS-FA, RB-MBs	[30,35,43,94,101,131,140]
Thermal decomposition	Fe-TiO <sub>2</sub> NDs	[41]
Encapsulation	DOX/Mn-TPPS@RBCs, GMCDs-FA@CMC, CPDP NPs, RBC-HPBs/HMME/PFH, FHMP NPs, (QD@P) Rs, MG@P NPs, IHG@P NPs, LIP3, OI_NPs, OIX_NP, AIMP NPs, IR780-NDs, FA-OINPs, mTiO <sub>2</sub> @PPYs, F3-PLGA@MB/Gd NPs, MnTTP-HSAs, PIO_NPs	[25,39,51,70,93,100,120,121,124,130,141,143–146,150,155,156]
Loading	GOx-MnO <sub>2</sub> /HMME, TPZ/HMTNPs-SNO	[40,74]
High-temperature organic-solution	Fe-VS <sub>2</sub> NSs	[134]
Grow on the surface	UPFB	[119]
High-temperature pyrolysis and oxidative exfoliation	OCN-PEG-(Ce6-Gd <sup>3+</sup> )/BNN6	[34]

gene is inserted directly into the cell's DNA, the imaging is generated only in the living cell and can retain accurate imaging for a long time as the cell divides and is passed on to daughter cells.<sup>163,164</sup> Various molecular imaging modalities, including FLI, PAI and MRI, could be used for reporter gene imaging for gene activity monitoring, cell tracing and gene therapy monitoring. The combination of sonosensitizer and reporter gene imaging technology could simultaneously play a role in the precise localization of cancer cells and gene therapy. This new therapy model may hold great promise.

## Conclusions and Outlook

There is no doubt that SDT has become a perfect cancer treatment due to its excellent therapeutic effectiveness, deep tissue penetration and low lateral injury. Since SDT was initially described in 1989, significant efforts have been made to use SDT for cancer treatment and to produce relevant sonosensitizers. Now, SDT combined imaging has opened the door to a new therapeutic approach and has become an attractive trend. Such multifunctional, integrated nanosystems are considered a potential candidate for innovative non-invasive therapeutics, presenting a prominent bright spot for enhancing nanosystems' applicability in the biomedical area. Imaging technology helps diagnose cancer earlier and more correctly, provides precise and potent therapy interventions for tumours, and improves prognosis and survival. Considering the limitations of existing therapies, SDT combination therapy may have higher clinical potential. Hence, creating new sonosensitizers with better diagnostic capabilities, especially those active solely in TME, maybe a prospective approach in sonodynamic research.

However, from a clinical point of view, there are still many elements to optimize the imaging quality. In order to further the research and development of tumour imaging and acoustic power integrated therapy, we must focus on novel imaging target identification and validation and investigate other features. Imaging probe production and characterization require the development of high sensitivity, high-resolution imaging equipment, hybrid equipment and improved image reconstruction techniques. Academic researchers, doctors, and the pharmaceutical sector must collaborate closely to bring integrated tumour imaging and dynamic treatment probes into cancer management.

We assume that by emphasizing the most recent achievements in this field, we can stimulate the scientific community to make significant contributions to cancer therapy. Based on the promising advances described in this research, we anticipate that these integrated nanoparticles for detection and therapy will shortly provide a new perspective for cancer therapeutic development.

## Funding

This review was supported by the National Natural Science Foundation of China (grant number 81873900 and 82171947).

## Disclosure

The authors report no conflicts of interest in this work.

## References

1. Sung H, Ferlay J, Siegel RL, et al. Global cancer statistics 2020: GLOBOCAN estimates of incidence and mortality worldwide for 36 cancers in 185 countries. *CA Cancer J Clin.* 2021;71(3):209–249. doi:10.3322/caac.21660
2. Fan W, Yung B, Huang P, Chen X. Nanotechnology for multimodal synergistic cancer therapy. *Chem Rev.* 2017;117(22):13566–13638. doi:10.1021/acs.chemrev.7b00258
3. Zheng Y, Ye J, Li Z, Chen H, Gao Y. Recent progress in sono-photodynamic cancer therapy: from developed new sensitizers to nanotechnology-based efficacy-enhancing strategies. *Acta Pharm Sin B.* 2021;11(8):2197–2219. doi:10.1016/j.apsb.2020.12.016
4. McHale AP, Callan JF, Nomikou N, Fowley C, Callan B. Sonodynamic therapy: concept, mechanism and application to cancer treatment. *Adv Exp Med Biol.* 2016;880:429–450. doi:10.1007/978-3-319-22536-4\_22
5. Wan GY, Liu Y, Chen BW, Liu YY, Wang YS, Zhang N. Recent advances of sonodynamic therapy in cancer treatment. *Cancer Biol Med.* 2016;13(3):325–338. doi:10.20892/j.issn.2095-3941.2016.0068
6. Liang S, Deng X, Ma P, Cheng Z, Lin J. Recent advances in nanomaterial-assisted combinational sonodynamic cancer therapy. *Adv Mater.* 2020;32(47):e2003214. doi:10.1002/adma.202003214
7. Chen H, Zhou X, Gao Y, Zheng B, Tang F, Huang J. Recent progress in development of new sonosensitizers for sonodynamic cancer therapy. *Drug Discov Today.* 2014;19(4):502–509. doi:10.1016/j.drudis.2014.01.010
8. Choi V, Rajora MA, Zheng G. Activating drugs with sound: mechanisms behind sonodynamic therapy and the role of nanomedicine. *Bioconjug Chem.* 2020;31(4):967–989. doi:10.1021/acs.bioconjchem.0c00029



9. Wu Y, Liu X, Qin Z, Hu L, Wang X. Low-frequency ultrasound enhances chemotherapy sensitivity and induces autophagy in PTX-resistant PC-3 cells via the endoplasmic reticulum stress-mediated PI3K/Akt/mTOR signaling pathway. *Onco Targets Ther.* **2018**;11:5621–5630. doi:10.2147/OTT.S176744
10. Bunevicius A, Pikis S, Padilla F, Prada F, Sheehan J. Sonodynamic therapy for gliomas. *J Neurooncol.* **2021**. doi:10.1007/s11060-021-03807-6
11. Um W, Ko H, You DG, et al. Necroptosis-inducible polymeric nanobubbles for enhanced cancer sonoimmunotherapy. *Adv Mater.* **2020**;32(16):e1907953. doi:10.1002/adma.201907953
12. Yang W, Xu H, Liu Q, et al. 5-Aminolevulinic acid hydrochloride loaded microbubbles-mediated sonodynamic therapy in pancreatic cancer cells. *Artif Cells Nanomed Biotechnol.* **2020**;48(1):1178–1188. doi:10.1080/21691401.2020.1813743
13. Liu M, Khan AR, Ji J, Lin G, Zhao X, Zhai G. Crosslinked self-assembled nanoparticles for chemo-sonodynamic combination therapy favoring antitumor, antimetastasis management and immune responses. *J Control Release.* **2018**;290:150–164. doi:10.1016/j.jconrel.2018.10.007
14. Zhao J, Shi J, Meng X, et al. ROS-Activated nanoscale coordination polymers for enhanced ultrasound-mediated therapy for the treatment of cancer. *Acta Biomater.* **2022**;143:372–380. doi:10.1016/j.actbio.2022.02.030
15. Zada S, Lu H, Yang F, et al. V2C nanosheets as dual-functional antibacterial agents. *ACS Appl Bio Mater.* **2021**;4(5):4215–4223. doi:10.1021/acsbm.1c00008
16. Huang P, Qian X, Chen Y, et al. Metalloporphyrin-encapsulated biodegradable nanosystems for highly efficient magnetic resonance imaging-guided sonodynamic cancer therapy. *J Am Chem Soc.* **2017**;139(3):1275–1284. doi:10.1021/jacs.6b11846
17. Qian X, Zheng Y, Chen Y. Micro/nanoparticle-augmented Sonodynamic Therapy (SDT): breaking the depth shallow of photoactivation. *Adv Mater.* **2016**;28(37):8097–8129. doi:10.1002/adma.201602012
18. Zhu P, Chen Y, Shi J. Nanoenzyme-augmented cancer sonodynamic therapy by catalytic tumor oxygenation. *ACS Nano.* **2018**;12(4):3780–3795. doi:10.1021/acsnano.8b00999
19. Pan X, Bai L, Wang H, et al. Metal-organic-framework-derived carbon nanostructure augmented sonodynamic cancer therapy. *Adv Mater.* **2018**;30(23):e1800180. doi:10.1002/adma.201800180
20. Zhang K, Chen H, Li F, et al. A continuous tri-phase transition effect for HIFU-mediated intravenous drug delivery. *Biomaterials.* **2014**;35(22):5875–5885. doi:10.1016/j.biomaterials.2014.03.043
21. Zeng L, Ma G, Lin J, Huang P. Photoacoustic probes for molecular detection: recent advances and perspectives. *Small.* **2018**;14(30):e1800782. doi:10.1002/sml.201800782
22. Cheng L, Shen S, Shi S, et al. FeSe<sub>2</sub>-decorated Bi<sub>2</sub>Se<sub>3</sub> nanosheets fabricated via cation exchange for chelator-free (64) Cu-labeling and multimodal image-guided photothermal-radiation therapy. *Adv Funct Mater.* **2016**;26(13):2185–2197. doi:10.1002/adfm.201504810
23. Maslov K, Zhang HF, Hu S, Wang LV. Optical-resolution photoacoustic microscopy for in vivo imaging of single capillaries. *Opt Lett.* **2008**;33(9):929–931.
24. Tian Y, Liu Y, Wang L, et al. Gadolinium-doped hollow silica nanospheres loaded with curcumin for magnetic resonance imaging-guided synergistic cancer sonodynamic-chemotherapy. *Mater Sci Eng C Mater Biol Appl.* **2021**;126:112157. doi:10.1016/j.msec.2021.112157
25. Zhang RY, Cheng K, Xuan Y, et al. A pH/ultrasonic dual-response step-targeting enterosoluble granule for combined sonodynamic-chemotherapy guided via gastrointestinal tract imaging in orthotopic colorectal cancer. *Nanoscale.* **2021**;13(7):4278–4294. doi:10.1039/d0nr08100k
26. Lim EK, Kim T, Paik S, Haam S, Huh YM, Lee K. Nanomaterials for theranostics: recent advances and future challenges. *Chem Rev.* **2015**;115(1):327–394. doi:10.1021/cr300213b
27. Smith BR, Gambhir SS. Nanomaterials for in vivo imaging. *Chem Rev.* **2017**;117(3):901–986. doi:10.1021/acs.chemrev.6b00073
28. Zhang HK, Chen Y, Kang J, et al. Prostate-specific membrane antigen-targeted photoacoustic imaging of prostate cancer in vivo. *J Biophotonics.* **2018**;11(9):e201800021. doi:10.1002/jbio.201800021
29. Liu F, He X, Liu L, You H, Zhang H, Wang Z. Conjugation of NaGdF<sub>4</sub> upconverting nanoparticles on silica nanospheres as contrast agents for multi-modality imaging. *Biomaterials.* **2013**;34(21):5218–5225. doi:10.1016/j.biomaterials.2013.03.058
30. Geng P, Yu N, Zhang J, et al. One responsive stone, three birds: mn(III)-hemoporphin frameworks with glutathione-enhanced degradation, MRI, and sonodynamic therapy. *Adv Healthc Mater.* **2021**;10(3):e2001463. doi:10.1002/adhm.202001463
31. Yuan P, Song D. MRI tracing non-invasive TiO<sub>2</sub>-based nanoparticles activated by ultrasound for multi-mechanism therapy of prostatic cancer. *Nanotechnology.* **2018**;29(12):125101. doi:10.1088/1361-6528/aaa92a
32. Warntjes JB, Leinhard OD, West J, Lundberg P. Rapid magnetic resonance quantification on the brain: optimization for clinical usage. *Magn Reson Med.* **2008**;60(2):320–329. doi:10.1002/mrm.21635
33. Andica C, Hagiwara A, Hori M, et al. Review of synthetic MRI in pediatric brains: basic principle of MR quantification, its features, clinical applications, and limitations. *J Neuroradiol.* **2019**;46(4):268–275. doi:10.1016/j.neurad.2019.02.005
34. Zheng Y, Liu Y, Wei F, et al. Functionalized g-C<sub>3</sub>N<sub>4</sub> nanosheets for potential use in magnetic resonance imaging-guided sonodynamic and nitric oxide combination therapy. *Acta Biomater.* **2021**;121:592–604. doi:10.1016/j.actbio.2020.12.011
35. Geng P, Yu N, Liu X, et al. Sub 5 nm Gd(3+) -hemoporphin framework nanodots for augmented sonodynamic theranostics and fast renal clearance. *Adv Healthc Mater.* **2021**;10(18):e2100703. doi:10.1002/adhm.202100703
36. Gong F, Cheng L, Yang N, et al. Ultrasmall oxygen-deficient bimetallic oxide MnWO<sub>x</sub> nanoparticles for depletion of endogenous GSH and enhanced sonodynamic cancer therapy. *Adv Mater.* **2019**;31(23):e1900730. doi:10.1002/adma.201900730
37. Deng Q, Sun P, Zhang L, et al. Porphyrin MOF Dots-based, function-adaptive nanoplatfor for enhanced penetration and photodynamic eradication of bacterial biofilms. *Adv Funct Mater.* **2019**;29(30). doi:10.1002/adfm.201903018
38. Zhang Y, Zhang L, Wang Z, et al. Renal-clearable ultrasmall covalent organic framework nanodots as photodynamic agents for effective cancer therapy. *Biomaterials.* **2019**;223:119462. doi:10.1016/j.biomaterials.2019.119462
39. Du B, Yan X, Ding X, et al. Oxygen self-production red blood cell carrier system for MRI mediated cancer therapy: ferryl-Hb, sonodynamic, and chemical therapy. *ACS Biomater Sci Eng.* **2018**;4(12):4132–4143. doi:10.1021/acsbomaterials.8b00497
40. Zhang Y, Wang H, Jia X, Du S, Yin Y, Zhang X. Cascade catalytic nanoplatfor for enhanced starvation and sonodynamic therapy. *J Drug Target.* **2020**;28(2):195–203. doi:10.1080/1061186X.2019.1641507
41. Bai S, Yang N, Wang X, et al. Ultrasmall iron-doped titanium oxide nanodots for enhanced sonodynamic and chemodynamic cancer therapy. *ACS Nano.* **2020**;14(11):15119–15130. doi:10.1021/acsnano.0c05235

42. Xie Q, Zeng D, Zhao Q, et al. Robust low-dose CT sinogram preprocessing via exploiting noise-generating mechanism. *IEEE Trans Med Imaging*. 2017;36(12):2487–2498. doi:10.1109/TMI.2017.2767290
43. Cheng K, Zhang RY, Yang XQ, et al. One-for-all nanoplatform for synergistic mild cascade-potentiated ultrasound therapy induced with targeting imaging-guided photothermal therapy. *ACS Appl Mater Interfaces*. 2020;12(36):40052–40066. doi:10.1021/acsami.0c10475
44. Lu X, Dou C, Fabiilli ML, Miller DL. Capillary hemorrhage induced by contrast-enhanced diagnostic ultrasound in rat intestine. *Ultrasound Med Biol*. 2019;45(8):2133–2139. doi:10.1016/j.ultrasmedbio.2019.04.012
45. Claudon M, Dietrich CF, Choi BI, et al. Guidelines and good clinical practice recommendations for Contrast Enhanced Ultrasound (CEUS) in the liver - update 2012: a WFUMB-EFSUMB initiative in cooperation with representatives of AFSUMB, AIUM, ASUM, FLAUS and ICUS. *Ultrasound Med Biol*. 2013;39(2):187–210. doi:10.1016/j.ultrasmedbio.2012.09.002
46. Huynh E, Rajora MA, Zheng G. Multimodal micro, nano, and size conversion ultrasound agents for imaging and therapy. *Wiley Interdiscip Rev Nanomed Nanobiotechnol*. 2016;8(6):796–813. doi:10.1002/wnan.1398
47. Rychak JJ, Klibanov AL, Ley KF, Hossack JA. Enhanced targeting of ultrasound contrast agents using acoustic radiation force. *Ultrasound Med Biol*. 2007;33(7):1132–1139. doi:10.1016/j.ultrasmedbio.2007.01.005
48. Sun S, Xu Y, Fu P, et al. Ultrasound-targeted photodynamic and gene dual therapy for effectively inhibiting triple negative breast cancer by cationic porphyrin lipid microbubbles loaded with HIF1 $\alpha$ -siRNA. *Nanoscale*. 2018;10(42):19945–19956. doi:10.1039/c8nr03074j
49. Tang H, Zheng Y, Chen Y. Materials chemistry of nanoultrasonic biomedicine. *Adv Mater*. 2017;29(10). doi:10.1002/adma.201604105
50. Song Z, Wang Z, Shen J, Xu S, Hu Z. Nerve growth factor delivery by ultrasound-mediated nanobubble destruction as a treatment for acute spinal cord injury in rats. *Int J Nanomedicine*. 2017;12:1717–1729. doi:10.2147/IJN.S128848
51. Zhang Q, Wang W, Shen H, et al. Low-intensity focused ultrasound-augmented multifunctional nanoparticles for integrating ultrasound imaging and synergistic therapy of metastatic breast cancer. *Nanoscale Res Lett*. 2021;16(1):73. doi:10.1186/s11671-021-03532-z
52. Seda R, Li DS, Fowlkes JB, Bull JL. Characterization of bioeffects on endothelial cells under acoustic droplet vaporization. *Ultrasound Med Biol*. 2015;41(12):3241–3252. doi:10.1016/j.ultrasmedbio.2015.07.019
53. Ho YJ, Yeh CK. Theranostic performance of acoustic nanodroplet vaporization-generated bubbles in tumor intertissue. *Theranostics*. 2017;7(6):1477–1488. doi:10.7150/thno.19099
54. Sheeran PS, Matsunaga TO, Dayton PA. Phase-transition thresholds and vaporization phenomena for ultrasound phase-change nanoemulsions assessed via high-speed optical microscopy. *Phys Med Biol*. 2013;58(13):4513–4534. doi:10.1088/0031-9155/58/13/4513
55. Kang ST, Lin YC, Yeh CK. Mechanical bioeffects of acoustic droplet vaporization in vessel-mimicking phantoms. *Ultrason Sonochem*. 2014;21(5):1866–1874. doi:10.1016/j.ulsonch.2014.03.007
56. Strohm E, Rui M, Gorelikov I, Matsuura N, Kolios M. Vaporization of perfluorocarbon droplets using optical irradiation. *Biomed Opt Express*. 2011;2(6):1432–1442.
57. Deng L, Cai X, Sheng D, et al. A laser-activated biocompatible theranostic nanoagent for targeted multimodal imaging and photothermal therapy. *Theranostics*. 2017;7(18):4410–4423. doi:10.7150/thno.21283
58. Ho YJ, Chang YC, Yeh CK. Improving nanoparticle penetration in tumors by vascular disruption with acoustic droplet vaporization. *Theranostics*. 2016;6(3):392–403. doi:10.7150/thno.13727
59. Yang C, Zhang Y, Luo Y, et al. Dual ultrasound-activatable nanodroplets for highly-penetrative and efficient ovarian cancer theranostics. *J Mater Chem B*. 2020;8(3):380–390. doi:10.1039/c9tb02198a
60. Ho YJ, Wu CH, Jin QF, et al. Superhydrophobic drug-loaded mesoporous silica nanoparticles capped with beta-cyclodextrin for ultrasound image-guided combined antivasculature and chemo-sonodynamic therapy. *Biomaterials*. 2020;232:119723. doi:10.1016/j.biomaterials.2019.119723
61. Zhang XH, Quinn A, Ducker WA. Nanobubbles at the interface between water and a hydrophobic solid. *Langmuir*. 2008;24(9):4756–4764.
62. Checco A, Hofmann T, DiMasi E, Black CT, Ocko BM. Morphology of air nanobubbles trapped at hydrophobic nanopatterned surfaces. *Nano Lett*. 2010;10(4):1354–1358. doi:10.1021/nl9042246
63. Peng H, Hampton MA, Nguyen AV. Nanobubbles do not sit alone at the solid-liquid interface. *Langmuir*. 2013;29(20):6123–6130. doi:10.1021/la305138v
64. Yildirim A, Chattaraj R, Blum NT, Goodwin AP. Understanding acoustic cavitation initiation by porous nanoparticles: toward nanoscale agents for ultrasound imaging and therapy. *Chem Mater*. 2016;28(16):5962–5972. doi:10.1021/acs.chemmater.6b02634
65. Yildirim A, Chattaraj R, Blum NT, Goldscheiter GM, Goodwin AP. Stable encapsulation of air in mesoporous silica nanoparticles: fluorocarbon-free nanoscale ultrasound contrast agents. *Adv Healthc Mater*. 2016;5(11):1290–1298. doi:10.1002/adhm.201600030
66. Thomas RG, Jonnalagadda US, Kwan JJ. Biomedical applications for gas-stabilizing solid cavitation agents. *Langmuir*. 2019;35(31):10106–10115. doi:10.1021/acs.langmuir.9b00795
67. Chen X, Kong L, Dong D, et al. Fabrication of functionalized copper compound hierarchical structure with bionic superhydrophobic properties. *J Phys Chem C*. 2009;113(14):5396–5401.
68. Zang D, Wu C, Zhu R, Zhang W, Yu X, Zhang Y. Porous copper surfaces with improved superhydrophobicity under oil and their application in oil separation and capture from water. *Chem Commun*. 2013;49(75):8410–8412. doi:10.1039/c3cc43536a
69. Jin Q, Lin CY, Kang ST, et al. Superhydrophobic silica nanoparticles as ultrasound contrast agents. *Ultrason Sonochem*. 2017;36:262–269. doi:10.1016/j.ulsonch.2016.12.001
70. Zhang H, Chen J, Zhu X, et al. Ultrasound induced phase-transition and invisible nanobomb for imaging-guided tumor sonodynamic therapy. *J Mater Chem B*. 2018;6(38):6108–6121. doi:10.1039/c8tb01788c
71. Singh R, Hussein GA, Pitt WG. Phase transitions of nanoemulsions using ultrasound: experimental observations. *Ultrason Sonochem*. 2012;19(5):1120–1125. doi:10.1016/j.ulsonch.2012.02.005
72. Paefgen V, Doleschel D, Kiessling F. Evolution of contrast agents for ultrasound imaging and ultrasound-mediated drug delivery. *Front Pharmacol*. 2015;6:197. doi:10.3389/fphar.2015.00197
73. Sheeran PS, Daghighi Y, Yoo K, et al. Image-guided ultrasound characterization of volatile sub-micron phase-shift droplets in the 20–40 MHz frequency range. *Ultrasound Med Biol*. 2016;42(3):795–807. doi:10.1016/j.ultrasmedbio.2015.11.012
74. Feng Q, Li Y, Yang X, et al. Hypoxia-specific therapeutic agents delivery nanotheranostics: a sequential strategy for ultrasound mediated on-demand tritherapies and imaging of cancer. *J Control Release*. 2018;275:192–200. doi:10.1016/j.jconrel.2018.02.011

75. Fan W, Bu W, Zhang Z, et al. X-ray radiation-controlled NO-release for on-demand depth-independent hypoxic radiosensitization. *Angew Chem Int Ed Engl*. 2015;54(47):14026–14030. doi:10.1002/anie.201504536
76. Zhang L, Wang D, Yang K, et al. Mitochondria-targeted artificial “Nano-RBCs” for amplified synergistic cancer phototherapy by a single NIR irradiation. *Adv Sci*. 2018;5(8):1800049. doi:10.1002/advs.201800049
77. Valluru KS, Wilson KE, Willmann JK. Photoacoustic imaging in oncology: translational preclinical and early clinical experience. *Radiology*. 2016;280(2):332.
78. Wilson KE, Wang TY, Willmann JK. Acoustic and photoacoustic molecular imaging of cancer. *J Nucl Med*. 2013;54(11):1851–1854. doi:10.2967/jnumed.112.115568
79. Yu J, Nguyen HNY, Steenbergen W, Kim K. Recent development of technology and application of photoacoustic molecular imaging toward clinical translation. *J Nucl Med*. 2018;59(8):1202–1207. doi:10.2967/jnumed.117.201459
80. Knox HJ, Hedhli J, Kim TW, Khalili K, Dobrucki LW, Chan J. A bioreducible N-oxide-based probe for photoacoustic imaging of hypoxia. *Nat Commun*. 2017;8(1):1794. doi:10.1038/s41467-017-01951-0
81. Wang LV. Multiscale photoacoustic microscopy and computed tomography. *Nat Photonics*. 2009;3(9):503–509. doi:10.1038/nphoton.2009.157
82. Schouw HM, Huisman LA, Janssen YF, et al. Targeted optical fluorescence imaging: a meta-narrative review and future perspectives. *Eur J Nucl Med Mol Imaging*. 2021;48(13):4272–4292. doi:10.1007/s00259-021-05504-y
83. Chen C, Tian R, Zeng Y, Chu C, Liu G. Activatable fluorescence probes for “turn-on” and ratiometric biosensing and bioimaging: from NIR-I to NIR-II. *Bioconjug Chem*. 2020;31(2):276–292. doi:10.1021/acs.bioconjchem.9b00734
84. Li K, Liu B. Polymer-encapsulated organic nanoparticles for fluorescence and photoacoustic imaging. *Chem Soc Rev*. 2014;43(18):6570–6597. doi:10.1039/c4cs00014e
85. Nguyen QT, Tsien RY. Fluorescence-guided surgery with live molecular navigation—a new cutting edge. *Nat Rev Cancer*. 2013;13(9):653–662. doi:10.1038/nrc3566
86. Troyan SL, Kianzad V, Gibbs-Strauss SL, et al. The FLARE intraoperative near-infrared fluorescence imaging system: a first-in-human clinical trial in breast cancer sentinel lymph node mapping. *Ann Surg Oncol*. 2009;16(10):2943–2952. doi:10.1245/s10434-009-0594-2
87. van Dam GM, Themelis G, Crane LM, et al. Intraoperative tumor-specific fluorescence imaging in ovarian cancer by folate receptor- $\alpha$  targeting: first in-human results. *Nat Med*. 2011;17(10):1315–1319. doi:10.1038/nm.2472
88. Zhu A, Miao K, Deng Y, et al. Dually pH/reduction-responsive vesicles for ultrahigh-contrast fluorescence imaging and thermo-chemotherapy-synergized tumor ablation. *ACS nano*. 2015;9(8):7874–7885.
89. Fan Q, Cheng K, Hu X, et al. Transferring biomarker into molecular probe: melanin nanoparticle as a naturally active platform for multimodality imaging. *J Am Chem Soc*. 2014;136(43):15185–15194. doi:10.1021/ja505412p
90. Zhang R, Fan Q, Yang M, et al. Engineering melanin nanoparticles as an efficient drug-delivery system for imaging-guided chemotherapy. *Adv Mater*. 2015;27(34):5063–5069. doi:10.1002/adma.201502201
91. Longo DL, Stefania R, Callari C, et al. Water soluble melanin derivatives for dynamic contrast enhanced photoacoustic imaging of tumor vasculature and response to antiangiogenic therapy. *Adv Healthc Mater*. 2017;6(1). doi:10.1002/adhm.201600550
92. Zhang L, Sheng D, Wang D, et al. Bioinspired multifunctional melanin-based nanoliposome for photoacoustic/magnetic resonance imaging-guided efficient photothermal ablation of cancer. *Theranostics*. 2018;8(6):1591–1606. doi:10.7150/thno.22430
93. Huang J, Liu F, Han X, et al. Nanosonosensitizers for highly efficient sonodynamic cancer theranostics. *Theranostics*. 2018;8(22):6178–6194. doi:10.7150/thno.29569
94. Dong C, Jiang Q, Qian X, et al. A self-assembled carrier-free nanosonosensitizer for photoacoustic imaging-guided synergistic chemo-sonodynamic cancer therapy. *Nanoscale*. 2020;12(9):5587–5600. doi:10.1039/c9nr10735e
95. Zhang B, Wang H, Shen S, et al. Fibrin-targeting peptide CREKA-conjugated multi-walled carbon nanotubes for self-amplified photothermal therapy of tumor. *Biomaterials*. 2016;79:46–55. doi:10.1016/j.biomaterials.2015.11.061
96. Lv W, Shen Y, Yang H, et al. A novel bimodal imaging agent targeting HER2 molecule of breast cancer. *J Immunol Res*. 2018;2018:6202876. doi:10.1155/2018/6202876
97. James NS, Chen Y, Joshi P, et al. Evaluation of polymethine dyes as potential probes for near infrared fluorescence imaging of tumors: part - 1. *Theranostics*. 2013;3(9):692–702. doi:10.7150/thno.5922
98. Gui R, Sun J, Liu D, Wang Y, Jin H. A facile cation exchange-based aqueous synthesis of highly stable and biocompatible Ag(2)S quantum dots emitting in the second near-infrared biological window. *Dalton Trans*. 2014;43(44):16690–16697. doi:10.1039/c4dt00699b
99. Duman FD, Erkisa M, Khodadust R, Ari F, Ulukaya E, Acar HY. Folic acid-conjugated cationic Ag2S quantum dots for optical imaging and selective doxorubicin delivery to HeLa cells. *Nanomedicine*. 2017;12(19):2319–2333.
100. Li C, Yang X-Q, An J, et al. Red blood cell membrane-enveloped O 2 self-supplementing biomimetic nanoparticles for tumor imaging-guided enhanced sonodynamic therapy. *Theranostics*. 2020;10(2):867–879. doi:10.7150/thno.37930
101. Zheng X, Liu W, Ge J, et al. Biodegradable natural product-based nanoparticles for near-infrared fluorescence imaging-guided sonodynamic therapy. *ACS Appl Mater Interfaces*. 2019;11(20):18178–18185.
102. Zheng X, Ge J, Wu J, et al. Biodegradable hypocrellin derivative nanovesicle as a near-infrared light-driven theranostic for dually photoactive cancer imaging and therapy. *Biomaterials*. 2018;185:133–141. doi:10.1016/j.biomaterials.2018.09.021
103. Ou Z, Liu G, Gao Y, et al. The effect of amphiphilic polymers on the association, morphology and photophysical properties of hypocrellin coordination polymer/fullerene assemblies. *Photochem Photobiol Sci*. 2014;13(11):1529–1540. doi:10.1039/c4pp00027g
104. Cai W, Chen X. Multimodality molecular imaging of tumor angiogenesis. *J Nucl Med*. 2008;49 Suppl 2:113S–28S. doi:10.2967/jnumed.107.045922
105. Louie A. Multimodality imaging probes: design and challenges. *Chem Rev*. 2010;110(5):3146–3195. doi:10.1021/cr9003538
106. Sun H, Zhang B, Jiang X, et al. Radiolabeled ultra-small Fe3O4 nanoprobe for tumor-targeted multimodal imaging. *Nanomedicine*. 2019;14(1):5–17.
107. Fan S, Zhang Y, Tan H, et al. Manganese/iron-based nanoprobe for photodynamic/chemotherapy combination therapy of tumor guided by multimodal imaging. *Nanoscale*. 2021;13(10):5383–5399. doi:10.1039/d0nr08831e
108. Ni J, Xu H, Zhong Y, Zhou Y, Hu S. Activatable UCL/CT/MR-enhanced in vivo imaging-guided radiotherapy and photothermal therapy. *J Mater Chem B*. 2022;10(4):549–561. doi:10.1039/d1tb02006d

109. Sheng D, Liu T, Deng L, et al. Perfluorooctyl bromide & indocyanine green co-loaded nanoliposomes for enhanced multimodal imaging-guided phototherapy. *Biomaterials*. 2018;165:1–13. doi:10.1016/j.biomaterials.2018.02.041
110. Jones LM, Dunham D, Rennie MY, et al. In vitro detection of porphyrin-producing wound bacteria with real-time fluorescence imaging. *Future Microbiol*. 2020;15(5):319–332.
111. Banala S, Fokong S, Brand C, et al. Quinone-fused porphyrins as contrast agents for photoacoustic imaging. *Chem Sci*. 2017;8(9):6176–6181. doi:10.1039/c7sc01369h
112. Ren Q, Yang K, Zou R, et al. Biodegradable hollow manganese/cobalt oxide nanoparticles for tumor theranostics. *Nanoscale*. 2019;11(47):23021–23026. doi:10.1039/c9nr07725a
113. Wang Y, Wu W, Liu J, et al. Cancer-cell-activated photodynamic therapy assisted by Cu(II)-based metal-organic framework. *ACS Nano*. 2019;13(6):6879–6890. doi:10.1021/acsnano.9b01665
114. Wan SS, Cheng Q, Zeng X, Zhang XZ. A Mn(III)-sealed metal-organic framework nanosystem for redox-unlocked tumor theranostics. *ACS Nano*. 2019;13(6):6561–6571. doi:10.1021/acsnano.9b00300
115. Zhang K, Meng X, Yang Z, Dong H, Zhang X. Enhanced cancer therapy by hypoxia-responsive copper metal-organic frameworks nanosystem. *Biomaterials*. 2020;258:120278. doi:10.1016/j.biomaterials.2020.120278
116. Wang J, Zhong Y, Wang X, et al. pH-dependent assembly of porphyrin–silica nanocomposites and their application in targeted photodynamic therapy. *Nano Lett*. 2017;17(11):6916–6921. doi:10.1021/acs.nanolett.7b03310
117. Yu B, Wei H, He Q, et al. Efficient uptake of (177) Lu-Porphyrin-PEG nanocomplexes by tumor mitochondria for multimodal-imaging-guided combination therapy. *Angew Chem Int Ed Engl*. 2018;57(1):218–222. doi:10.1002/anie.201710232
118. Shao S, Rajendiran V, Lovell JF. Metalloporphyrin nanoparticles: coordinating diverse theranostic functions. *Coord Chem Rev*. 2019;379:99–120. doi:10.1016/j.ccr.2017.09.002
119. Wang Z, Liu B, Sun Q, et al. Upconverted metal-organic framework janus architecture for near-infrared and ultrasound co-enhanced high performance tumor therapy. *ACS Nano*. 2021. doi:10.1021/acsnano.1c04280
120. Wang J, Huang J, Zhou W, et al. Hypoxia modulation by dual-drug nanoparticles for enhanced synergistic sonodynamic and starvation therapy. *J Nanobiotechnol*. 2021;19(1):87. doi:10.1186/s12951-021-00837-0
121. Ma A, Chen H, Cui Y, et al. Metalloporphyrin complex-based nanosensitizers for deep-tissue tumor theranostics by noninvasive sonodynamic therapy. *Small*. 2019;15(5):e1804028. doi:10.1002/sml.201804028
122. Lei P, An R, Zheng X, et al. Ultrafast synthesis of ultrasmall polyethylenimine-protected AgBiS2 nanodots by “rookie method” for in vivo dual-modal CT/PA imaging and simultaneous photothermal therapy. *Nanoscale*. 2018;10(35):16765–16774. doi:10.1039/c8nr04870c
123. Chen B, Zhang C, Wang W, et al. Ultrastable AgBiS2 hollow nanospheres with cancer cell-specific cytotoxicity for multimodal tumor therapy. *ACS Nano*. 2020;14(11):14919–14928. doi:10.1021/acsnano.0c04370
124. Zhang R, Zhang L, Ran H, et al. A mitochondria-targeted anticancer nanoplatfrom with deep penetration for enhanced synergistic sonodynamic and starvation therapy. *Biomater Sci*. 2020;8(16):4581–4594. doi:10.1039/d0bm00408a
125. Yan S, Lu M, Ding X, et al. HematoPorphyrin Monomethyl Ether polymer contrast agent for ultrasound/photoacoustic dual-modality imaging-guided synergistic high intensity focused ultrasound (HIFU) therapy. *Sci Rep*. 2016;6:31833. doi:10.1038/srep31833
126. Gao H, Wang Z, Tan M, et al. pH-responsive nanoparticles for enhanced antitumor activity by high-intensity focused ultrasound therapy combined with sonodynamic therapy. *Int J Nanomed*. 2022;17:333–350. doi:10.2147/IJN.S336632
127. Kuang Y, Zhang K, Cao Y, et al. Hydrophobic IR-780 dye encapsulated in cRGD-conjugated solid lipid nanoparticles for NIR imaging-guided photothermal therapy. *ACS Appl Mater Interfaces*. 2017;9(14):12217–12226. doi:10.1021/acsami.6b16705
128. Yang Z, Cheng R, Zhao C, et al. Thermo- and pH-dual responsive polymeric micelles with upper critical solution temperature behavior for photoacoustic imaging-guided synergistic chemo-photothermal therapy against subcutaneous and metastatic breast tumors. *Theranostics*. 2018;8(15):4097–4115. doi:10.7150/thno.26195
129. Alves CG, Lima-Sousa R, de Melo-Diogo D, Louro RO, Correia IJ. IR780 based nanomaterials for cancer imaging and photothermal, photodynamic and combinatorial therapies. *Int J Pharm*. 2018;542(1–2):164–175. doi:10.1016/j.ijpharm.2018.03.020
130. Zhao XZ, Zhang W, Cao Y, et al. A cleverly designed novel lipid nanosystem: targeted retention, controlled visual drug release, and cascade amplification therapy for mammary carcinoma in vitro. *Int J Nanomed*. 2020;15:3953–3964. doi:10.2147/IJN.S244743
131. Hou R, Liang X, Li X, Zhang X, Ma X, Wang F. In situ conversion of rose bengal microbubbles into nanoparticles for ultrasound imaging guided sonodynamic therapy with enhanced antitumor efficacy. *Biomater Sci*. 2020;8(9):2526–2536. doi:10.1039/c9bm02046b
132. Soldani C, Croce AC, Bottone MG, et al. Apoptosis in tumour cells photosensitized with Rose Bengal acetate is induced by multiple organelle photodamage. *Histochem Cell Biol*. 2007;128(5):485–495. doi:10.1007/s00418-007-0333-3
133. Bottiroli G, Croce AC, Balzarini P, et al. Enzyme-assisted cell photosensitization: a proposal for an efficient approach to tumor therapy and diagnosis. The Rose Bengal Fluorogenic Substrate. *Photochem Photobiol*. 1997;66(3):374–383.
134. Lei H, Wang X, Bai S, et al. Biodegradable Fe-Doped vanadium disulfide theranostic nanosheets for enhanced sonodynamic/chemodynamic therapy. *ACS Appl Mater Interfaces*. 2020;12(47):52370–52382. doi:10.1021/acsami.0c14647
135. Chen Y, Cheng L, Dong Z, et al. Degradable vanadium disulfide nanostructures with unique optical and magnetic functions for cancer theranostics. *Angew Chem Int Ed Engl*. 2017;56(42):12991–12996. doi:10.1002/anie.201707128
136. Cheng L, Yuan C, Shen S, et al. Bottom-Up synthesis of metal-ion-doped WS(2) nanoflakes for cancer theranostics. *ACS Nano*. 2015;9(11):11090–11101. doi:10.1021/acsnano.5b04606
137. Porcu EP, Salis A, Gavini E, Rassu G, Maestri M, Giunchedi P. Indocyanine green delivery systems for tumour detection and treatments. *Biotechnol Adv*. 2016;34(5):768–789. doi:10.1016/j.biotechadv.2016.04.001
138. Chen J, Liu C, Zeng G, et al. Indocyanine green loaded reduced graphene oxide for in vivo photoacoustic/fluorescence dual-modality tumor imaging. *Nanoscale Res Lett*. 2016;11(1):85. doi:10.1186/s11671-016-1288-x
139. Gao C, Deng ZJ, Peng D, et al. Near-infrared dye-loaded magnetic nanoparticles as photoacoustic contrast agent for enhanced tumor imaging. *Cancer Biol Med*. 2016;13(3):349–359. doi:10.20892/j.issn.2095-3941.2016.0048
140. Yang Y, Fan Z, Zheng K, et al. A novel self-targeting theranostic nanoplatfrom for photoacoustic imaging-monitored and enhanced chemo-sonodynamic therapy. *J Mater Chem B*. 2021;9(27):5547–5559. doi:10.1039/d1tb01025e



141. Chen S, Liu Y, Zhu S, et al. Dual-mode imaging and therapeutic effects of drug-loaded phase-transition nanoparticles combined with near-infrared laser and low-intensity ultrasound on ovarian cancer. *Drug Deliv.* 2018;25(1):1683–1693. doi:10.1080/10717544.2018.1507062
142. Wilson K, Homan K, Emelianov S. Biomedical photoacoustics beyond thermal expansion using triggered nanodroplet vaporization for contrast-enhanced imaging. *Nat Commun.* 2012;3:618. doi:10.1038/ncomms1627
143. Xie W, Zhu S, Yang B, et al. The destruction of laser-induced phase-transition nanoparticles triggered by low-intensity ultrasound: an innovative modality to enhance the immunological treatment of ovarian cancer cells. *Int J Nanomed.* 2019;14:9377–9393. doi:10.2147/IJN.S208404
144. Zheng J, Sun J, Chen J, et al. Oxygen and oxaliplatin-loaded nanoparticles combined with photo-sonodynamic inducing enhanced immunogenic cell death in syngeneic mouse models of ovarian cancer. *J Control Release.* 2021;332:448–459. doi:10.1016/j.jconrel.2021.02.032
145. Liu Y, Chen S, Sun J, et al. Folate-targeted and oxygen/indocyanine green-loaded lipid nanoparticles for dual-mode imaging and photo-sonodynamic/photothermal therapy of ovarian cancer in vitro and in vivo. *Mol Pharm.* 2019;16(10):4104–4120. doi:10.1021/acs.molpharmaceut.9b00339
146. He Y, Wan J, Yang Y, et al. Multifunctional polypyrrole-coated mesoporous TiO<sub>2</sub> nanocomposites for photothermal, sonodynamic, and chemotherapeutic treatments and dual-modal ultrasound/photoacoustic imaging of tumors. *Adv Healthcare Mater.* 2019;8(9). doi:10.1002/adhm.201801254
147. Kesa P, Purova M, Babic M, et al. Photoacoustic properties of polypyrrole nanoparticles. *Nanomaterials.* 2021;11(9). doi:10.3390/nano11092457
148. Men X, Yuan Z. Multifunctional conjugated polymer nanoparticles for photoacoustic-based multimodal imaging and cancer photothermal therapy. *J Innov Opt Health Sci.* 2019;12(03). doi:10.1142/s1793545819300015
149. de Sousa LE, de Paiva LS, da Silva Filho DA, Sini G, de Oliveira Neto PH. Assessing the effects of increasing conjugation length on exciton diffusion: from small molecules to the polymeric limit. *J Physical Chemistry Chemical Physics.* 2021;23(29):15635–15644. doi:10.1039/d1cp01263k
150. Li Y, Hao L, Liu F, et al. Cell penetrating peptide-modified nanoparticles for tumor targeted imaging and synergistic effect of sonodynamic/HIFU therapy. *Int J Nanomed.* 2019;14:5875–5894. doi:10.2147/IJN.S212184
151. Sahu A, Choi WI, Lee JH, Tae G. Graphene oxide mediated delivery of methylene blue for combined photodynamic and photothermal therapy. *Biomaterials.* 2013;34(26):6239–6248. doi:10.1016/j.biomaterials.2013.04.066
152. He LL, Wang X, Wu XX, et al. Protein damage and reactive oxygen species generation induced by the synergistic effects of ultrasound and methylene blue. *Spectrochim Acta A Mol Biomol Spectrosc.* 2015;134:361–366. doi:10.1016/j.saa.2014.06.121
153. Morgounova E, Shao Q, Hackel BJ, Thomas DD, Ashkenazi S. Photoacoustic lifetime contrast between methylene blue monomers and self-quenched dimers as a model for dual-labeled activatable probes. *J Biomed Opt.* 2013;18(5):56004. doi:10.1117/1.JBO.18.5.056004
154. Xiang J, Leung AW, Xu C. Effect of ultrasound sonication on clonogenic survival and mitochondria of ovarian cancer cells in the presence of methylene blue. *J Ultrasound Med.* 2014;33(10):1755–1761. doi:10.7863/ultra.33.10.1755
155. Liu S, Zhang W, Chen Q, et al. Multifunctional nanozyme for multimodal imaging-guided enhanced sonodynamic therapy by regulating the tumor microenvironment. *Nanoscale.* 2021;13(33):14049–14066. doi:10.1039/d1nr01449h
156. Zhang L, Yi H, Song J, et al. Mitochondria-targeted and ultrasound-activated nanodroplets for enhanced deep-penetration sonodynamic cancer therapy. *ACS Appl Mater Interfaces.* 2019;11(9):9355–9366. doi:10.1021/acsami.8b21968
157. Meng X, Wang H, Yang M, et al. Target-cell-specific bioorthogonal and endogenous ATP control of signal amplification for intracellular MicroRNA imaging. *Anal Chem.* 2021;93(3):1693–1701. doi:10.1021/acs.analchem.0c04302
158. Chen Y, Shang H, Wang C, et al. RNA-Seq explores the mechanism of oxygen-boosted sonodynamic therapy based on all-in-one nanobubbles to enhance ferroptosis for the treatment of HCC. *Int J Nanomed.* 2022;17:105–123. doi:10.2147/IJN.S343361
159. Shang H, Chen Y, Wang C, et al. RNA-Seq technology reveals the mechanism of SDT combined with novel nanobubbles against HCC. *Front Mol Biosci.* 2021;8:791331. doi:10.3389/fmolb.2021.791331
160. Wu B, Yuan Y, Liu J, et al. Single-cell RNA sequencing reveals the mechanism of sonodynamic therapy combined with a RAS inhibitor in the setting of hepatocellular carcinoma. *J Nanobiotechnol.* 2021;19(1):177. doi:10.1186/s12951-021-00923-3
161. Yin H, Sun L, Pu Y, et al. Ultrasound-controlled CRISPR/Cas9 system augments sonodynamic therapy of hepatocellular carcinoma. *ACS Cent Sci.* 2021;7(12):2049–2062. doi:10.1021/acscentsci.1c01143
162. Li M, Wang Y, Liu M, Lan X. Multimodality reporter gene imaging: construction strategies and application. *Theranostics.* 2018;8(11):2954–2973. doi:10.7150/thno.24108
163. Acton PD, Zhou R. Imaging reporter genes for cell tracking with PET and SPECT. *Q J Nucl Med Mol Imaging.* 2005;49(4):349.
164. van der Bogt KE, Swijnenburg RJ, Cao F, Wu JC. Molecular imaging of human embryonic stem cells: keeping an eye on differentiation, tumorigenicity and immunogenicity. *Cell Cycle.* 2006;5(23):2748–2752. doi:10.4161/cc.5.23.3533